PHYSICAL REVIEW B **87**, 085107 (2013)

Heisenberg antiferromagnet on Cayley trees: Low-energy spectrum and even/odd site imbalance

Hitesh J. Changlani,[1] Shivam Ghosh,[1] Christopher L. Henley,[1] and Andreas M. Läuchli[2]
[1]*Laboratory of Atomic and Solid State Physics, Cornell University, Ithaca, New York 14853, USA*
[2]*Institut für Theoretische Physik, Universität Innsbruck, A-6020 Innsbruck, Austria*

(Received 14 September 2012; revised manuscript received 28 December 2012; published 6 February 2013)

To understand the role of local sublattice imbalance in low-energy spectra of $s = \frac{1}{2}$ quantum antiferromagnets, we study the $s = \frac{1}{2}$ quantum nearest neighbor Heisenberg antiferromagnet on the coordination 3 Cayley tree. We perform many-body calculations using an implementation of the density matrix renormalization group (DMRG) technique for generic tree graphs. We discover that the bond-centered Cayley tree has a quasidegenerate set of a low-lying tower of states and an "anomalous" singlet-triplet finite-size gap scaling. For understanding the construction of the first excited state from the many-body ground state, we consider a wave function ansatz given by the single-mode approximation, which yields a high overlap with the DMRG wave function. Observing the ground-state entanglement spectrum leads us to a picture of the low-energy degrees of freedom being "giant spins" arising out of sublattice imbalance, which helps us analytically understand the scaling of the finite-size spin gap. The Schwinger-boson mean-field theory has been generalized to *nonuniform* lattices, and ground states have been found which are spatially inhomogeneous in the mean-field parameters.

DOI: 10.1103/PhysRevB.87.085107 PACS number(s): 75.10.Jm, 75.10.Dg, 05.10.Cc

I. INTRODUCTION

Quantum antiferromagnetism for unfrustrated systems has been one of the most extensively researched subjects in condensed matter physics. One of the simplest models in this family, the nearest neighbor spin-$\frac{1}{2}$ Heisenberg antiferromagnet on the square lattice, has been studied extensively: analytically with spin-wave[1–3] and Schwinger-boson approaches[4–8] and numerically with quantum Monte Carlo[9] (which has no "sign problem" for bipartite lattices). That said, effects from physical imperfections such as the presence of open edges[10,11] and static nonmagnetic impurities[12] are less well understood and hence are areas of active research.

In this paper, we study quantum antiferromagnetism on the Cayley tree (or Bethe lattice[13]), a bipartite lattice without loops, with the motivation of understanding the low-energy spectrum of the spin-1/2 Heisenberg model on this lattice. The Cayley tree has the well-known general pathology that in the thermodynamic limit, the number of boundary sites is a finite fraction of the total number of sites; as a consequence, different ways of approaching the thermodynamic limit may give different results in any problem based on the Cayley tree. A particular manifestation of this for the antiferromagnet is that finite trees may have a large excess of sites belonging to one sublattice over the other.

Our systematic study of the low-energy spectrum of the spin-1/2 Heisenberg Hamiltonian on the Cayley tree shows that the effect of sublattice imbalance is to create a "tower of states" lower than the Anderson tower of states.[14–18] A similar result was obtained by Wang and Sandvik[19] from their study of spin-1/2 antiferromagnets on diluted square lattices. Aided by numerical calculations, we propose a framework for understanding this effect. We also find that Schwinger-boson mean-field theory[5] is a good description of the many-body ground state and can reproduce many of its features quantitatively.

Previous studies of this model by Otsuka[20] and Friedman[21] focused primarily on ground-state properties, and excited states were not considered in these studies. More recently Kumar *et al.*[22] have significantly extended this analysis to both the spin-1/2 and spin-1 Heisenberg model. We use all these studies as useful benchmarks for our own numerical calculations.

From a theorist's perspective, the Cayley tree achieves many simplifications which make exact solutions possible; e.g., the Bose Hubbard model on this lattice was recently solved by Semerijan, Tarzia, and Zamponi.[24] It is also the basis of approximations such as the Brinkman-Rice treatment of the Hubbard model.[25] More recently, it found applications in the treatment of the quantum impurity problem which is at the heart of dynamical mean-field theory (DMFT).[26] It does not appear that a spin model has been realized on such a topology experimentally (though there has been interest in the study of dendrimers[27–29]).

In our case, the complete absence of loops makes this lattice conducive for the density matrix renormalization group (DMRG) algorithm.[30] With the DMRG method we have an explicit (yet compact) representation of ground- and excited-state many-body wave functions which gives us abundant information to understand the low-energy properties of these systems. In particular, reduced density matrices can be used as tools to understand properties of these states.[31]

The remainder of the paper is divided as follows. In Sec. II we introduce the model and lattices being investigated and define a measure of sublattice imbalance associated with them. In Sec. III, we give a brief overview of our implementation of the DMRG algorithm applied to generic trees. In Sec. IV, we discuss the general properties of the ground state and excited states of the bond-centered Cayley tree. In Sec. V, we use a variational ansatz given by the single-mode approximation, in conjunction with an argument from first-order perturbation theory, to explain the finite-size scaling of the spin gap. Finally, in Sec. VI, we corroborate our observations of the ground-state properties, by the use of the Schwinger-boson mean-field theory (SBMFT).

II. THE MODEL

We consider the nearest neighbor antiferromagnetic spin-$1/2$ Heisenberg model with uniform coupling J,

$$H = J \sum_{\langle i,j \rangle} \mathbf{S}_i \cdot \mathbf{S}_j . \tag{2.1}$$

In this paper, we use the spin rotational symmetry of the Hamiltonian (2.1) to label many-body states by $|S, S_z\rangle$, where S refers to the spin of the state and S_z is its z component. On a bipartite lattice (with sublattices A and B), like the Cayley tree, with n_A sites in sublattice A and n_B sites in sublattice B, it is rigorously known[32] that the ground state of the Heisenberg Hamiltonian has a net spin $S = |\frac{n_A - n_B}{2}|$.

The first kind of tree we consider is the "bond-centered" Cayley tree of the form depicted in Fig. 1(a). The number of sites N_s for such a cluster is related to the "generation" g by

$$N_s(g) = 2^{g+1} - 2. \tag{2.2}$$

Since the bond-centered clusters have no "global imbalance," i.e., $n_A = n_B$, the ground state is a singlet (and the monotonicity of the energy with total spin S implies that the first excited state is a triplet).

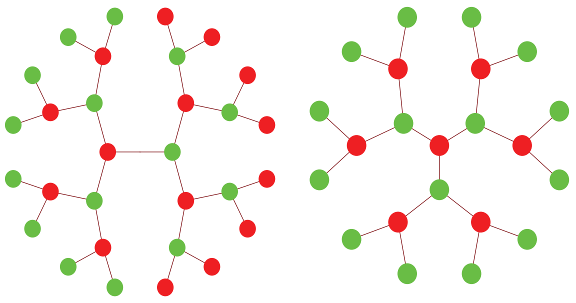

(a) Bond centered (b) Site centered

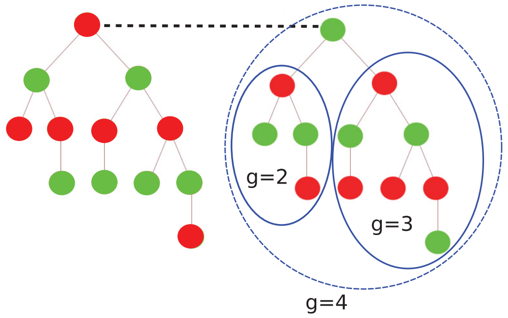

(c) Fibonacci

FIG. 1. (Color online) (a) The bond-centered Cayley tree. (b) The site-centered Cayley tree. In both cases all sites, other than those on the boundary, have coordination 3. (c) The "Fibonacci Cayley tree" is constructed hierarchically and has some coordination 2 sites. The figure shows a generation 4 cluster constructed by connecting the roots (head sites) of the generation 2 and generation 3 trees to a common site (the root of the generation 4 tree). To have a globally balanced cluster we introduced a bond connecting the root of the generation 4 tree with the root of its mirror image. All clusters in (a), (b), and (c) are bipartite [the dark (red) and light (green) colors show the two sublattices] and have no loops.

As mentioned before, the notion of "local sublattice imbalance" will be crucial in understanding the low-energy physics. For the bond-centered cluster, we define a measure of imbalance (which we refer to as I_b from here on) by dividing the cluster at the central bond into two equal parts. We count the excess of one sublattice over the other in one half of the cluster and multiply by 1/2 for spin-$1/2$. It can be easily shown that $I_b(g)$ is related to the generation g as

$$I_b(g) = \frac{2^g \pm 1}{6}, \tag{2.3}$$

where $+$ $(-)$ is for g odd (even).

Figure 1(b) is the more usual way of defining a Cayley tree and which we refer to as "site-centered." The number of sites is related to the generation g by

$$N_s(g) = 3(2^g - 1) + 1. \tag{2.4}$$

Unlike the bond-centered cluster, a global sublattice imbalance exists here which leads to a ground-state spin of $S_0 \equiv 2^{g-1}$. We measure the imbalance $I_s(g)$ in either of the three symmetrical arms of the site-centered Cayley tree: Specifically, we count the excess sites of one sublattice over the other (in one arm) and multiply by 1/2. This definition is particularly convenient as it gives us $I_s(g) = I_b(g)$ for all g.

A recent publication on the study of the Heisenberg model on the Cayley tree by Kumar, Ramasesha, and Soos[22] considers the site-centered clusters. We confirm their results for the site-centered case, but interestingly find that the bond-centered cluster has significantly different ground- and excited-state properties. We will provide some brief comparisons in Sec. IV to illustrate this point.

How is the situation different if there is no imbalance locally? To address this, we introduce the "Fibonacci Cayley tree." The recipe for constructing the generation $g+1$ Fibonacci Cayley tree is to combine the generation g and $g-1$ trees by connecting their roots (head sites) to a common site [which in turn serves as the root (head site) of the generation $g+1$ tree]. Figure 1(c) illustrates this construction.

If we label the number of odd and even sublattice sites by A_g and B_g, respectively, then (counting the root as even) we get

$$A_{g+1} = 1 + B_g + B_{g-1}, \tag{2.5a}$$
$$B_{g+1} = A_g + A_{g-1}. \tag{2.5b}$$

The total number of sites N_s at generation $g+1$ is

$$\begin{aligned} N_s(g+1) &= A_{g+1} + B_{g+1} \\ &= 1 + B_g + B_{g-1} + A_g + A_{g-1} \\ &= 1 + N_s(g) + N_s(g-1). \end{aligned} \tag{2.6}$$

Observe that $N_s(g)$ satisfies the Fibonacci recursion, that is, $N_s(g) = F_{g+1} - 1$, where F_g is the gth Fibonacci number, which justifies the name of the tree. The size of this lattice grows as τ^g where τ is the golden ratio $\tau = (1+\sqrt{5})/2 \sim 1.618$. Also, every third generation is unbalanced by 1 and every other generation is both globally and locally balanced. Table I shows the sizes of the Fibonacci Cayley clusters along with the number of sites in the even and odd sublattices for up to $g = 11$ generations.

TABLE I. Number of sites in a Fibonacci Cayley tree as a function of generation g. A_g is number of A sublattice sites; $B_g = A_g$ except for the entries marked with $*$, in which case $B_g = A_g - 1$. The total count is $N_s(g) = A_g + B_g$.

g	0	1	2	3	4	5	6	7	8	9	10	11
A_g	1	1	2	4$*$	6	10	17*	27	44	72*	116	188
$N_s(g)$	1	2	4	7	12	20	33	54	88	143	232	376

In order to have a balanced cluster at every generation, we combine two identical generation g Fibonacci constructions [as in Eq. (2.6)] by introducing a bond connecting their roots as shown in Fig. 1(c).

III. DENSITY MATRIX RENORMALIZATION GROUP ON GENERIC TREE GRAPHS

The density matrix renormalization group (DMRG) is a powerful numerical technique for studying many-body systems. It was developed by White[30] for one-dimensional systems to remedy the problems associated with the numerical renormalization group (NRG).[33] DMRG has also been generalized to study lattice models (such as the spin-1/2 Heisenberg model[20–22] and the fermionic Hubbard[34] model) on the Cayley tree. More recently, Murg *et al.*[35] have also used the Cayley tree to embed quantum chemical systems to study them with tree tensor network algorithms (closely related to the DMRG).

When Otsuka[20] and Friedman[21] first adapted the DMRG to the Cayley tree, their procedure was for regular trees and utilized an infinite-system DMRG. A recent publication by Kumar *et al.*[22] (for the site-centered lattice) improves upon the scaling of previous algorithms, by considering an efficient way to hierarchically construct the lattice. Our implementation differs from all of the above, as it allows us to study the properties of *any* finite tree (and not necessarily regular ones, e.g., percolation clusters[36]). We outline the details in the remainder of this section.

We spell out the notation we have used in this section. d is the number of degrees of freedom per site. For example, $d = 2$ for a spin-1/2 Hamiltonian. z is the coordination number of a site (although our discussion talks in terms of uniform z, a generalization to site-dependent z is straightforward). M will be used to denote the number of retained states on a local cluster of sites (or "block").

A. Initialization

Our algorithm starts with the generation of a suitable guess wave function. As Fig. 2 shows, this is done by performing "energy-based truncations" of the Hilbert space on a successive hierarchy of clusters of sites (or "blocks"), assuming they are completely disconnected from the rest of the cluster. By "energy-based truncation" we mean that on each block we retain only the M lowest energy states of the local block Hamiltonian, where M is a parameter that determines the accuracy of the calculation.

This blocking procedure is carried out at various parts of the tree, beginning from the boundary sites of the cluster and terminating when one reaches the geometrically central point (called the "focal" point or "root"). Thus, at the end of the initialization calculation, one has a description of the Hamiltonian of the entire system in terms of the root degree of freedom surrounded by z blocks.

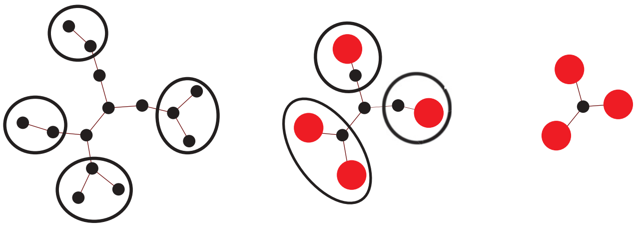

FIG. 2. (Color online) Warm-up step of the DMRG involving multiple independent renormalization procedures on the tree utilizing energy-based truncation. The "army continues to march in" from all sides till one reaches the geometrically central point (often called the "focal point" or "root"). Here we show all stages for a given tree. The red dots represent renormalized blocks.

While the end result of our calculations are expected to be independent of this initialization, a good choice for the starting guess wave function can greatly accelerate convergence. In particular, we modify our criterion for retaining states when targeting an excited state (say in a high-S_z sector). During the initialization we introduce a "fake" uniform magnetic field in the Hamiltonian to favor retention of states that describe the high-energy wave function.

B. Density matrix based truncation

We will now consider how every "iteration" in the DMRG is carried out to systematically approach the ground (or excited) state(s) of the system. For this purpose, we require a description of the full Hamiltonian in terms of a "site" degree of freedom [here (↑ , ↓)] and the basis spanned by the M^z states retained on the z blocks surrounding it.

At every iteration we use the Lanczos algorithm[37] to solve for the lowest energy eigenvector of the entire system (also referred to as the "superblock"). Then, treating one of the blocks as the "environment" and the remaining $z - 1$ blocks (the "systems") and the "site" collectively as the "new system", we obtain the reduced density matrix, ρ_{RDM}, of the "new system" from the ground state (ψ_{GS}) of the superblock by computing

$$\rho_{\mathrm{RDM}} \equiv \mathrm{Tr}_{\mathrm{env}}\left(|\psi_{\mathrm{GS}}\rangle\langle\psi_{\mathrm{GS}}|\right). \tag{3.1}$$

As is illustrated in Fig. 3, each block takes its turn being the "environment" while the other blocks (the "systems") together with the "site" act as the "new system". (The order of choosing environments is not very crucial to the final result.)

In addition to the ground-state density matrix, we have also targeted higher excited states, by performing a state averaging of the reduced density matrix,

$$\rho_{\mathrm{RDM}}^{\mathrm{avg}} \equiv \frac{\sum_i w_i \mathrm{Tr}_{\mathrm{env}}\left(|\psi_i\rangle\langle\psi_i|\right)}{\sum_i w_i}, \tag{3.2}$$

where w_i is the positive weight given to the density matrix formed from state $|\psi_i\rangle$. In most cases, we simply used $w_i = 1$ for all states we targeted. An advantage of state averaging is

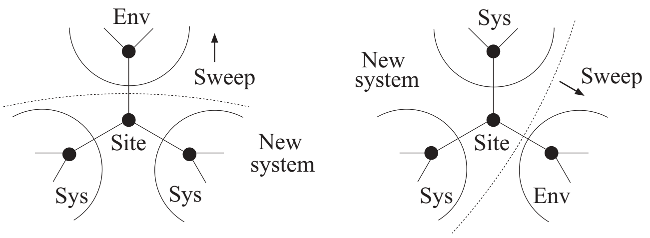

FIG. 3. Division of the Cayley tree locally into site, system(s), and environment as required by the DMRG. One renormalization step consists of combining the site and system(s) into a new system, retaining the states governed by tracing out the environment degrees of freedom.

that it often helps us to prevent (or get us out of) solutions which are local (but not global) minima. The reduced density matrix is diagonalized and only M states with the highest eigenvalues (out of the total dM^z states) are kept on the block.

C. Sweep algorithm

Once the density matrix based truncations with the root as "site" are completed, the algorithm proceeds to consider a new division of the lattice into "systems" and "environment" by considering a site on the shell one step out from the root. Each of the z sites connected to the original root gets its turn being the "new root". (See the arrows in Fig. 3 as an example of the directions in which the "sweep" algorithm proceeds).

After this stage, we consider the sites which are two steps away from the root of the tree (i.e., one step away from the previous sites used to divide the system). This "sweeping out" process continues till one reaches the exterior of the cluster. Once we reach the exterior of the cluster, we "sweep in," like we did during the initialization procedure. However, this time (and for all future sweeps) we have an environment present, whose states we trace over to guide the density matrix based truncation process. This in-out-in sweep continues till convergence of the energy is attained. One "complete sweep" is defined here as a "sweep out" (from the root to the boundaries) followed by a "sweep in" (from boundaries to the root) operation.

The scaling of algorithm (per sweep) can be understood as follows. Each Lanczos diagonalization of the superblock costs $M^z d$ amount of effort and there are N_s such diagonalizations needed, where N_s is the number of sites in the tree. For a highly symmetrical lattice (such as the Cayley tree), one can reduce this computational cost to $O(\ln(N_s)M^z d)$ (however this has not been implemented).

The reduced density matrix computed from the eigenvector of the superblock has dimensions $M^{z-1}d \times M^{z-1}d$, which costs $M^{3(z-1)}d^3$ amount of computational effort to diagonalize. However, one must keep in mind that this reduced density matrix has a block diagonal structure owing to the fact that the retained states have definite S_z symmetry, which brings down the cost associated with this step.

D. Computing expectations

Just as in the usual one-dimensional DMRG, we have an explicit representation of the wave function in terms of the block states and we can efficiently compute various kinds of correlation functions. For the purpose of this paper, we have simply measured the spin-spin correlation functions $\langle \mathbf{S}_i \cdot \mathbf{S}_j \rangle$ and the matrix element $\langle 1|S_i^+|0\rangle$, where $|0\rangle$ ($|1\rangle$) refers to the ground-state singlet (first excited state triplet) and has the labels $|S=0,S_z=0\rangle$ ($|S=1,S_z=1\rangle$). Both these functions are needed for calculating the coefficients occurring in the single-mode approximation, which will be discussed in Sec. V. The latter is computed by targeting the ground and excited state in the same DMRG run, so that both states have the same block representation.

TABLE II. Energy (E_{GS}) and Spin gap (Δ) for the 190-site site-centered and 176-site Fibonacci lattices for various values of M.

	$N_s = 190$		$N_s = 176$	
M	E_{GS}	Δ	E_{GS}	Δ
20	−74.54049387	0.9397293	−76.46983049	0.08834668
60	−74.54054021	0.9397198	−76.47071767	0.08725531
100	−74.54054022	0.9397198	−76.47072851	0.08725207

We also compute the eigenvalues of the reduced density matrix (for a particular division of the lattice), collectively known as the "entanglement spectrum." These turn out to be a very useful probe of the low-energy degrees of freedom (as we will see in Sec. V C). This needs no extra effort in the DMRG, since these eigenvalues are computed anyway as part of the Hilbert space truncation process.

E. Parameters and benchmarks

All calculations reported here are for trees with a maximum coordination of $z = 3$. For all systems considered here, the retained number of states M was less than or equal to 160 and we observed a reasonable convergence of the energy within 10–20 sweeps.

To benchmark our calculations we have also compared our results with exact-diagonalization data where possible. In particular, for the bond-centered tree we considered the ground-state energies and correlations in all S_z sectors of the 30-site cluster and some high-S_z sectors for the 62-site cluster.

One can see from Table II that the convergence of the energy (in the S_z sector corresponding to the spin S_0 of the ground state) and the spin gap (defined to be $E(S_0+1) - E(S_0)$) is rapid as a function of the number of retained states on a block (M) for the site centered and Fibonacci trees. However, for the bond centered tree (see Table III), the convergence with M

TABLE III. Energy (E_{GS}), Spin gap (Δ), and S^+ matrix elements for the central (c) and boundary (b) sites for the 126-site bond-centered tree for various values of M. $|0\rangle$ and $|1\rangle$ refer to the lowest singlet and triplet, respectively.

M	E_{GS}	Δ	$\langle 1\|S_c^+\|0\rangle$	$\langle 1\|S_b^+\|0\rangle$
60	−49.3405119	3.4×10^{-4}	0.310	0.370
80	−49.3412938	5.7×10^{-4}	0.300	0.344
100	−49.3415002	6.0×10^{-4}	0.280	0.337
120	−49.3415347	6.0×10^{-4}	0.279	0.335
140	−49.3415521	6.0×10^{-4}	0.278	0.335

is comparatively slower. Based on our data, we conclude that while larger M calculations are certainly desirable, the present calculations are reasonable and confirm the existence of a low (and anomalously scaling) energy scale in the many-body spectrum of the bond-centered tree.

The question of finite-size scaling can be considered tricky given the small magnitude of the singlet-triplet gap of the bond-centered clusters. However, by computing the ground-state energy in every S_z sector and fitting the "tower of states" (to be discussed in Sec. IV B), we believe the errors in estimation of this scaling behavior are mitigated.

IV. GROUND AND EXCITED STATES

Using the DMRG algorithm presented in Sec. III, we calculate the ground-state energy and spin gap and point out the differences between the bond- and site-centered clusters. To highlight the role of local imbalance, we also compare the excited states of the bond-centered and Fibonacci trees, both of which are globally balanced.

A. Ground-state energy, spin-spin correlations, and spin gap

We consider the bond-centered, site-centered, and Fibonacci clusters and compute the lowest energy $E_{GS}(S)$ for various spin sectors S. The notation S_0 will be used to refer to the spin of the ground state. In order to compute the ground-state energy per site in the infinite lattice limit e_0 we fit $E_{GS}(S_0)/N_s$ to the functional form

$$\frac{E_{GS}}{N_s} = e_o + \frac{a}{N_s} + \frac{b}{N_s^2}. \tag{4.1}$$

For bond-centered clusters we found $e_0 = -0.393855(2)$ and for the site-centered clusters $e_0 = -0.393854(2)$, both of which are consistent within error bars of extrapolation and with the value of $e_0 = -0.39385$ reported for site-centered clusters by Ref. 22.

In comparison, as Table IV shows, the energy per site of the Fibonacci tree is significantly lower than either of the bond- or site-centered trees. This is achieved by the formation of very strong nearest neighbor dimers (especially on the boundary, as the degree of dimerization dies down as one proceeds inwards). The degree of boundary dimerization is more limited in the site- and bond-centered trees. Despite the dissimilarities between the three lattices, the "bulk limit" of the estimated energy per bond, based on taking an average of nearest neighbor $\langle \mathbf{S}_i \cdot \mathbf{S}_j \rangle$ over the innermost bonds, is roughly identical for all three kinds of Cayley trees and equals about $-0.35J$.

TABLE IV. Ground-state energy per site (e_0), finite-size scaling parameters for the ground-state energy (a,b) [from Eq. (4.1)], and spin gap (Δ_{+1}) [from Eqs. (4.2), (4.3)] for the bond-centered, site-centered, and Fibonacci clusters. We also record the gap $\Delta_{-1} \equiv E_{GS}(S_0 - 1) - E_{GS}(S_0)$ for the site-centered cluster.

Cluster	$-e_0$	a	b	Δ_{+1}	Δ_{-1}
Bond centered	0.393855(2)	0.29	-1.0	$\sim N_s^{-2}$	
Site centered	0.393854(1)	0.29	$+0.1$	$0.73 + 2.86/N_s^{0.5}$	$2.19/N_s$
Fibonacci	0.435433(1)	0.17	-0.4	$\sim N_s^{-0.6}$	

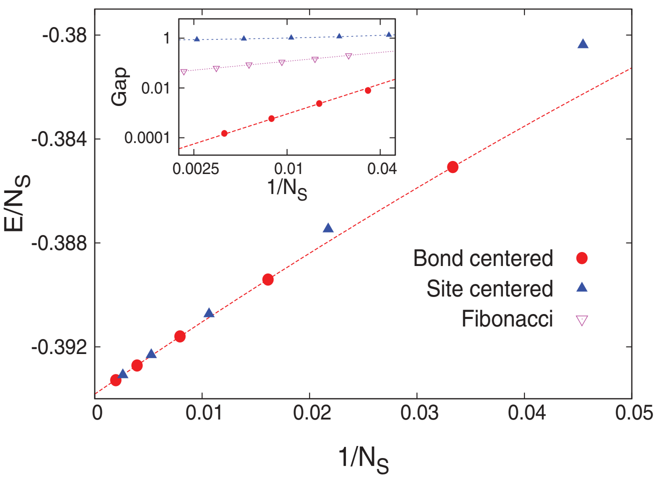

FIG. 4. (Color online) Ground-state energy per site for the bond-centered and site-centered Cayley trees for various lattice sizes. The Fibonacci Cayley tree energies are out of the scale considered. A fit to the bond-centered results given by Eq. (4.1) has been shown. Inset: Finite-size scaling of the energy gap Δ plotted on a log-log scale. The bond-centered and Fibonacci clusters appear gapless in the infinite lattice limit, with a finite-size scaling exponent of $\alpha \approx 2$ and $\alpha \approx 0.6$. However, the site-centered clusters have a finite Δ in the infinite lattice limit in concordance with the results of Ref. 22. The lines shown are fits to the DMRG data using Eqs. (4.2) and (4.3).

We now turn to a discussion of the spin gap. For the site-centered tree there are two possible spin gaps $\Delta(S_0 \rightarrow S_0 \pm 1)$ that can be considered, corresponding to $S_0 \rightarrow S_0 \pm 1$ magnetic transitions (as a shorthand we refer to these gaps as $\Delta_{\pm 1}$). In the limit of a small magnetic field, for finite system sizes, we get a discrete set of energy levels and the lowest excitation involving a single spin flip is $S_0 \rightarrow S_0 + 1$ transition. This excitation has a gap in the infinite lattice limit, which we obtained by fitting to

$$\Delta(S_0 \rightarrow S_0 + 1) = \Delta_\infty + \frac{c}{N_s^\alpha} \tag{4.2}$$

and found Δ_∞ to be 0.731(4) and $\alpha \sim 0.5$. Interestingly, the spin gap $\Delta(S_0 \rightarrow S_0 - 1)$ is found to be gapless in the thermodynamic limit as seen from the finite-size fit in Table IV.

The bond-centered and Fibonacci clusters appear to be gapless in the infinite lattice limit, based on cluster sizes up to 254 and 464 sites, respectively. We computed the finite-size scaling of this gap using

$$\Delta(0 \rightarrow 1) \sim N_s^{-\alpha}. \tag{4.3}$$

Empirically, the value of $\alpha \sim 0.6$ for Fibonacci and $\alpha \sim 2$ for the bond-centered clusters matches rather well with our data (see inset of Fig. 4).

Denoting the ground state as $|0\rangle$, we also compute the ground state connected correlation function defined here as

$$G_{ij} \equiv \langle 0|\mathbf{S}_i \cdot \mathbf{S}_j|0\rangle - \langle 0|S_i^z|0\rangle\langle 0|S_j^z|0\rangle. \tag{4.4}$$

For the bond-centered and Fibonacci clusters, $\langle 0|S_i^z|0\rangle = 0$ for all i, and hence we have

$$G_{ij} = \langle 0|\mathbf{S}_i \cdot \mathbf{S}_j|0\rangle. \tag{4.5}$$

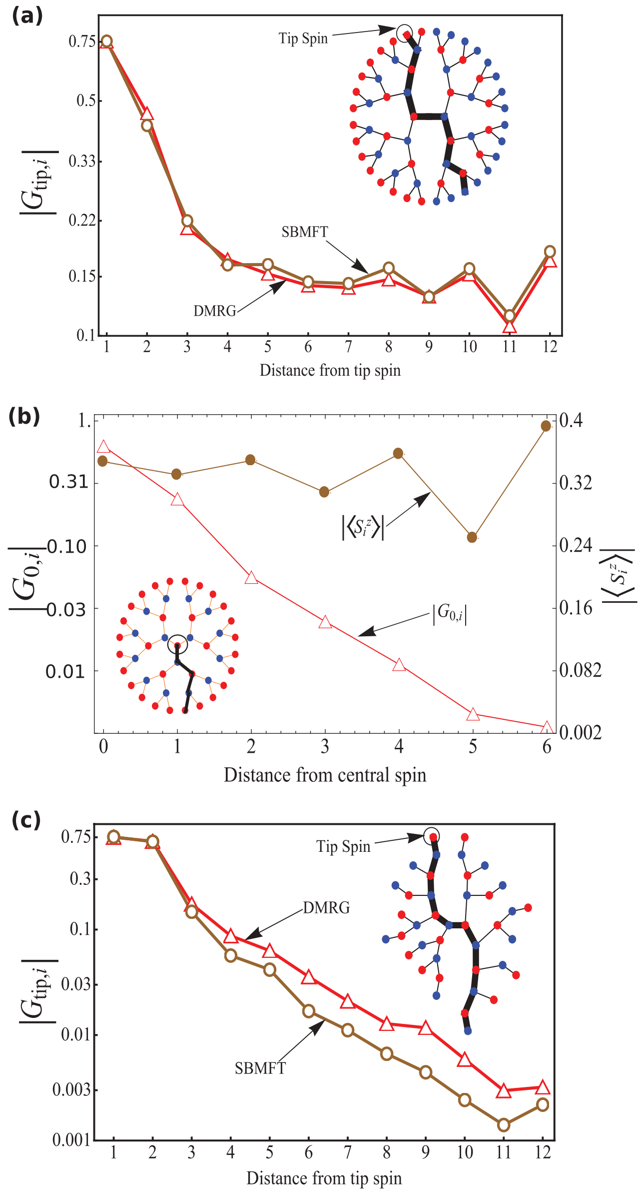

FIG. 5. (Color online) Ground-state spin-spin correlations $G_{a,i}$, as in Eq. (4.4), for the three kinds of Cayley tree. One (reference) spin a is held fixed while the other spin i is take at distance a along the highlighted path. In (a) and (c), the reference spin is at a tip ($a \to$ tip), and DMRG results are compared with numerical solutions of Schwinger-boson mean-field theory (SBMFT) from Sec. VI. In (b), the reference spin is at the central ("root") site ($a \to 0$). (a) Bond-centered tree with $N_s = 126$ sites. The SBMFT correlations shown have been scaled up by an overall factor of 1.8 to take into account corrections beyond mean field (in the broken-symmetry phase). The DMRG and SBMFT results show good agreement, asymptoting to a constant. (b) Site-centered cluster with $N_s = 190$ sites, in the maximum S_z member of the ground-state multiplet ($S_z = S_0$). The magnetization $|\langle S_i^z\rangle|$ is also shown, as a function of distance from the center. Even though the connected correlation function decays to zero exponentially fast, the long-range order is encoded in the fact that that the magnetization is nonzero. (c) Fibonacci tree with $N_s = 40$ sites. For the "quantum disordered" phase, the SBMFT correlations were scaled up by an overall factor of 3/2 (for details see Sec. VI B). Correlations appear to be decaying exponentially with distance.

Figure 5 shows some sample correlation functions on all three lattices. The marked difference in the behavior of the spin gap and the spin correlations between the site- and bond-centered clusters can be attributed to a different manifestation on the two types of clusters of the spontaneous spin symmetry breaking occurring in the thermodynamic limit. First, the behavior of the spin correlations can be understood in the following way: On the site-centered clusters, the system has an extensive total spin $S = 2^{g-1}$ in the ground state. By choosing a particular state out of this large multiplet it is possible to orient the Néel vector at no energy cost in this finite-size system. In particular, if one considers the $S^z = S$ state of the multiplet, the local $\langle S_i^z\rangle$ expectation values will reflect the ordering pattern directly. This situation is somewhat analogous to ferrimagnetic systems. In the case of the bond-centered clusters we have a unique $S = 0$ ground state, which forbids finite $\langle S_i^z\rangle$ expectation values on a finite system, and the long-range order then has to be coded in the correlation functions leveling off to a finite value at long distances.

B. Low-energy tower of states

For the balanced Heisenberg antiferromagnet ($n_A = n_B$ with a singlet ground state) on a regular unfrustrated lattice (e.g., square in 2D or cubic in 3D), with number of sites N_s, it has been noted and argued[17,18] that the low-energy Hamiltonian can be described by a rigid rotor model,

$$H_{\mathrm{rot}} = \frac{\mathbf{S}^2}{2I} = \frac{S(S+1)}{2I}, \tag{4.6}$$

where **S** it the total angular momentum (spin), and

$$I \cong \chi N_s, \tag{4.7}$$

where χ is the susceptibility of **S** to a field coupling to it. Thus, we have a sequence of multiplets, popularly referred to as the "Anderson tower of states," which become degenerate in the limit $N_s \to \infty$ thus making $SU(2)$ symmetry breaking possible in this limit. However, contrary to the effects of spontaneous spin rotational symmetry breaking on regular lattices, the Cayley tree does not have any Goldstone modes.[23]

To observe the Anderson tower of states on the Cayley tree, we compute the ground-state energy in every S_z sector. This may be identified with the multiplet energy $E(S)$, since $E(S)$ is monotonic in S and $S \geqslant S_z$.

For the bond-centered clusters, a tower of states exists, but an anomalous one. In Fig. 6 we observe that in the bond-centered case, the $E(S)$ curve consists of *two* linear pieces, joined at a critical spin S^* which depends on the cluster size. In effect, the system has two moments of inertia, I_{low} for $S < S^*$ and the (much smaller) I_{high} for $S > S^*$. Finite-size fits of the moment of inertia show that $I_{\mathrm{low}} \approx 0.191 N_s^2$ while $I_{\mathrm{high}} \approx 0.358 N_s$; it will be our task in Sec. V C to explain this difference. We also observe that

$$S^* = 2I_b, \tag{4.8}$$

where I_b is the sublattice imbalance on one half of the bond-centered cluster as defined in Eq. (2.3).

For the Fibonacci tree, we do not find a clear distinction between the two linear pieces as seen in Fig. 6. The scaling of the energy gaps $[E(S+1) - E(S)]$ changes from $N_s^{-0.6}$

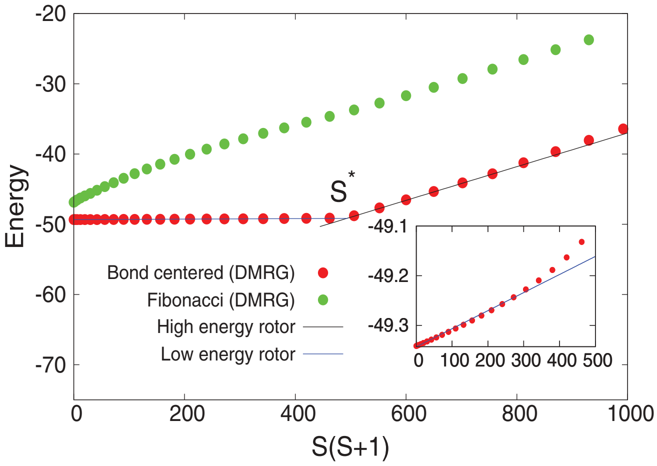

FIG. 6. (Color online) Lowest energy level in every S_z sector for the 108-site Fibonacci and the 126-site bond-centered Cayley trees. The range of S from 0 to S^* has been magnified and shown in the inset for the 126-site cluster. It shows a tower of states with a much larger moment of inertia than expected from the Anderson tower. This is seen as a sharp kinklike feature at S^*. In contrast, for the Fibonacci tree, the transition from the low to high S behavior is less well defined.

for small S to the $1/N_s$ Anderson scaling for large S. In contrast with the gapless spectrum of the bond-centered and Fibonacci clusters, the site-centered case has a finite spin gap (see Table IV) in the infinite lattice limit.

A complementary probe of the low-energy physics is the magnetization (m) defined as

$$m = \frac{1}{N_s}\sum_i \langle S_i^z\rangle_{GS}, \tag{4.9}$$

as a function of a uniform applied magnetic field h. For the bond-center clusters, we observe (see Fig. 7) a rapid increase in magnetization for small h and it seems the saturation magnetization is about $m^* \sim 1/6$ (i.e., $m^*/m_{\text{sat}} \sim 1/3$). Beyond this rapid rise of the magnetization at small field, the magnetization curve displays a surprisingly rich structure, with several plateau-like features at intermediate magnetization, linked by more susceptible parts of the magnetization curve. We note that the first plateau at m^* seems to have an extent in magnetic field similar to that for the site-centered clusters studied in Ref. 22. The detailed characterization of the magnetization curve as $N_s \to \infty$ appears to be an interesting problem for future studies.

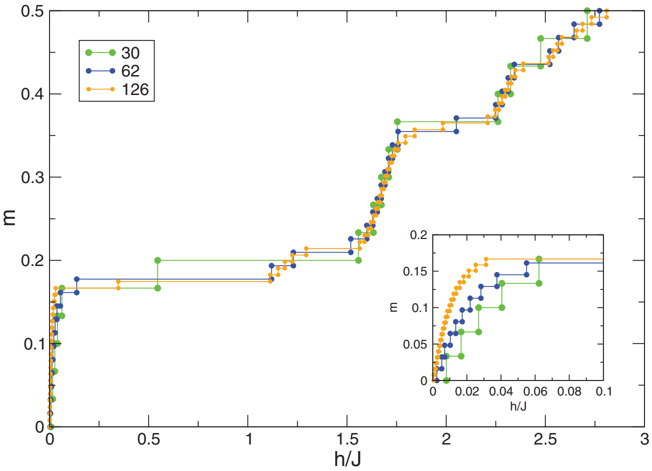

FIG. 7. (Color online) Magnetization curves for bond-centered Cayley trees of various sizes obtained using DMRG. Inset: The rapid rise of the magnetization with application of a small magnetic field indicates a susceptibility diverging with system size.

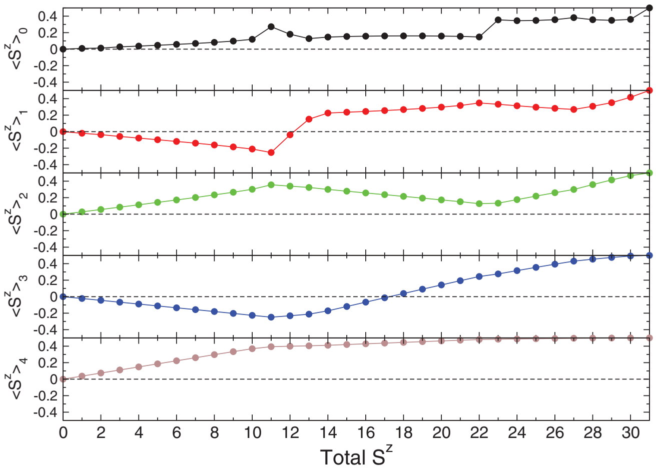

FIG. 8. (Color online) Magnetization curves for sites on various shells of the 62-site bond-centered Cayley tree. The subscript refers to the shell on which the site is present; that is, 0 refers to the central two sites and the 4 refers to the boundary.

In Fig. 8, we also show the magnetization curves for sites on various shells of the 62-site bond-centered Cayley tree. For small S_z (or equivalently small magnetic fields), we infer that while the boundary spins are most susceptible, the spins in the interior also have a comparably high susceptibility, which decreases as we go inwards.

V. SINGLE-MODE APPROXIMATION FOR THE EXCITED STATE

Can we understand the origin of the “anomalous” states in the low-energy spectrum for the bond-centered tree? In order to address this question, we study the nature of the triplet excited state and its relation to the ground state using the single-mode approximation[38] (SMA for short). Assuming the knowledge of the ground-state wave function $|0\rangle$ (analytically or from a numerical method), the SMA ansatz for the trial state $|1'\rangle \equiv |S = 1, S_z = 1\rangle$ state is given by

$$|1'\rangle = \frac{1}{\mathcal{N}_{1'}}\sum_{j=1}^{N_s} u_j S_j^+|0\rangle, \tag{5.1}$$

where u_j are variational parameters and $\mathcal{N}_{1'}$ is a normalization factor given by

$$\mathcal{N}_{1'} \equiv \sqrt{\sum_{k,l} u_k^* u_l \langle 0|S_k^- S_l^+|0\rangle}. \tag{5.2}$$

Using the spin symmetry of the Hamiltonian (and hence its eigenfunctions) and the fact that the ground state has $S_z = 0$, the normalization factor $\mathcal{N}_{1'}$ (5.2) can be written as

$$\mathcal{N}_{1'} = \sqrt{\sum_{k,l} \frac{2}{3} u_k u_l G_{kl}}, \tag{5.3}$$

where G_{kl} is the spin-spin correlation function previously defined in Eq. (4.5).

For a singlet ground state, observe that there is a gauge degree of freedom in the choice of the SMA wave function (5.1), an arbitrary constant shift u, i.e.,

$$\sum_i u_i S_i^+ |0\rangle = \sum_i (u_i + u) S_i^+ |0\rangle, \tag{5.4}$$

since for a ground state with total spin $S = 0$,

$$u \sum_i S_i^+ |0\rangle = u S_{\mathrm{tot}}^+ |0\rangle = 0. \tag{5.5}$$

It can also be shown[39] that the normalization $\mathcal{N}_{1'}$ in Eq. (5.3) is invariant under the transformation $u_i \to u_i + u$.

For a given trial state ψ_T which is a function of some parameters u_j, the variational principle guarantees that

$$E_T \equiv \frac{\langle \psi_T(\{u_j\}) | H | \psi_T(\{u_j\}) \rangle}{\langle \psi_T(\{u_j\}) | \psi_T(\{u_j\}) \rangle}, \tag{5.6}$$

where E_0 refers to the energy of the lowest lying state with the same symmetry as the trial wave function. The best wave function is obtained by optimization of parameters $\{u_j\}$ by minimizing the variational energy E_T. Note that within the SMA formalism, the ground state (and hence the ground-state energy) is assumed, which implies that the SMA spin gap is also a variational estimate for the true spin gap.

Here we will show that the SMA does turn out to be a very good ansatz for this system based on the close to 100% overlap of the SMA wave function with the wave function from DMRG. Our procedure does not require explicit knowledge of the wave function; rather only certain matrix elements and correlation functions are necessary. We will derive our intuition from numerical calculations; we construct coefficients u_j occurring in Eq. (5.1) to obtain a simple variational state with a gap that goes to 0 faster than $1/N_s$. The aim of this section is thus to understand the operator that creates the triplet wave function from the ground-state singlet. This in turn will tell us how the spins collectively act, which will be used to understand the existence of an "anomalous" energy scale.

A similar SMA calculation was performed by Laumann *et al.*,[40] who considered AKLT models on the Cayley tree, where the analytical form of the correlation functions is known. Instead, we use the values of $\langle 1 | S_i^+ | 0 \rangle$ and G_{ij} from our DMRG calculations as inputs for our analysis. In addition, we make no assumptions about the variational parameters $\{u_j\}$.

A. Obtaining the SMA coefficients from maximization of overlap with the true wave function

The overlap of an approximate wave function with the exact one can serve as a good measure of its quality. Thus we consider the overlap of the SMA wave function with the true triplet state $|1\rangle \equiv |S = 1, S_z = 1\rangle$, i.e.,

$$\begin{aligned} O &\equiv \langle 1 | 1'.\rangle \\ &= \frac{\sum_j u_j f_j}{\sqrt{\sum_{k,l} \frac{2}{3} u_k u_l G_{kl}}}, \end{aligned} \tag{5.7}$$

and try to maximize it. We have defined f_i to be

$$f_i \equiv \langle 1 | S_j^+ | 0 \rangle. \tag{5.8}$$

We christen this term the "flippability" of a spin. This is motivated from its very definition: The more easily flipped spins have a larger contribution to the formation of the first excited triplet.

Now we present a method to obtain the optimal parameters u_j to construct $|1'\rangle$. To meet the requirements of a high overlap of the SMA wave function $|1'\rangle$ with the exact many-body triplet $|1\rangle$, subject to the constraint that it is normalized, we devise a cost function C_{SMA}, defined as

$$C_{SMA} = -\sum_j u_j f_j + \lambda \left(\mathcal{N}_{1'}^2 - 1 \right), \tag{5.9}$$

where we have introduced λ as a Lagrange multiplier. Taking $\{u_j\}$ as our variational parameters, and setting the derivatives of C_{SMA} to 0, we get

$$\frac{\partial C_{SMA}}{\partial u_i} = -f_i + \frac{4}{3} \lambda \sum_{l \neq i} u_l G_{il} + \lambda u_i = 0. \tag{5.10}$$

Thus we get the set of equations (one equation for each i)

$$f_i = \frac{4}{3} \lambda \sum_j G_{ij} u_j. \tag{5.11}$$

To explicitly obtain a state $|1'\rangle$ which has a high overlap with $|1\rangle$, we solve the above linear equations for u_i numerically. Note that the matrix G always has exactly one zero eigenvalue because of the gauge degree of freedom (5.4). Hence we cannot simply invert G to obtain u_i; instead, we directly solve the linear system of equations (5.11) using DGESV in LAPACK.

A natural choice of gauge for the parameters $\{u_j\}$ is to satisfy

$$\sum_i u_i = 0. \tag{5.12}$$

Our observation from the numerical solution of Eq. (5.11) for the bond-centered Cayley tree is that $u_i > 0$ for i on one side of the central bond and $u_i < 0$ on the other side. We have also plotted the amplitudes of the optimal SMA coefficients for the 30, 62, and 126 site bond-centered Cayley trees in Fig. 9.

B. Comparison of various SMA wave functions

We next try to understand the qualitative nature of the SMA solution from the perspective of minimizing the triplet energy. We consider various functional forms for u_i and numerically compute their overlap with the exact triplet and compare SMA gap estimates.

For the nearest neighbor Heisenberg model, the SMA gap is given by (for a derivation refer to Appendix A)

$$\Delta_{SMA} = \frac{-\sum_{\langle k,l \rangle} (u_k - u_l)^2 G_{kl}}{2 \sum_{ij} u_i u_j G_{ij}}. \tag{5.13}$$

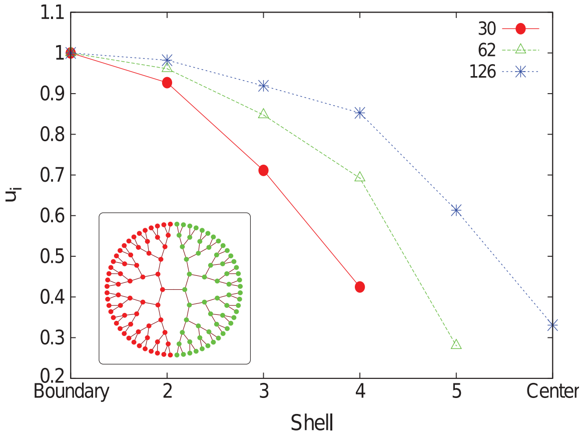

FIG. 9. (Color online) Amplitude of the SMA coefficients u_i for various shells (normalized with respect to amplitude on the boundary) for the $N_s = 30$, 62, and 126 site bond-centered lattices. Inset: The sign structure of u_i is the same as Eq. (5.14). Dark (red) and light (green) indicates negative and positive u_i, respectively.

Observe that the numerator and denominator (being proportional to $\mathcal{N}_{1'}^2$) are invariant under the transformation $u_i \rightarrow u_i + u$.

To minimize the SMA gap, one would like to minimize the numerator and maximize the denominator of Eq. (5.13) (note both the numerator and denominator are positive). To minimize the numerator, we can try to keep $u_k \approx u_l$ for as many bonds as possible, and hence consider the "left-right" ansatz,

$$u_i = \begin{cases} +1 & i \in \text{left of central bond,} \\ -1 & i \in \text{right of central bond,} \end{cases} \tag{5.14}$$

which is consistent with the gauge condition (5.12). This sign structure is in concordance with the numerical solution of Eqs. (5.11) for the bond-centered Cayley tree.

Note that this is quite contrary to the "staggered pattern" one obtains by solving Eqs. (5.11) for the square lattice. The staggered pattern is defined as

$$u_i = \begin{cases} +1 & i \in \text{even sublattice,} \\ -1 & i \in \text{odd sublattice.} \end{cases} \tag{5.15}$$

The staggered pattern is an energetically expensive solution for the bond-centered Cayley tree. Even though it maximizes the denominator making it $O(N_s^2)$, the numerator is also large, i.e., $O(N_s)$. Thus the SMA gap scales only as $O(1/N_s)$.

Table V verifies the arguments presented above by explicitly listing out the SMA gap and overlap with the exact wave function for the various choices of u_i we have considered here. Our inference is that the optimal and the "left-right" ansatz are qualitatively similar and yield a much smaller SMA gap than the "staggered" ansatz.

The SMA calculations suggest that all the spins are involved in the construction of the first excited state from the ground state. The u_i corresponding to the central spins is roughly a third of the u_i of the boundary spins in the "optimal solution" and exactly as much as the boundary spins in the "left-right" ansatz. The point to note here is that in either case the contribution of the spins in the interior is not small. This suggests that the antiferromagnetic bonds between successive shells do a reasonable job of locking spins together (within each half of the bond-centered tree), resulting in an emergent degree of freedom which is what we call a "giant spin." This interpretation will be established next in Sec. V C.

TABLE V. SMA gap and wave function overlap with excited state from DMRG for various functional forms of u_i

N_s	u_i	SMA Gap	Overlap
30	Optimal	0.0135	0.998
	Left-Right	0.0341	0.993
	Staggered	0.2680	0.912
62	Optimal	0.0039	0.999
	Left-Right	0.0116	0.997
	Staggered	0.1612	0.946
126	Optimal	0.0010	≈1
	Left-Right	0.0028	≈1
	Staggered	0.0905	0.975

C. The "giant spins" picture

As we inferred previously, there are indications that strong antiferromagnetic correlations force all spins in one half of the bond-centered cluster to act collectively as a single magnetic moment. We make this understanding more concrete in the present section.

We divide the bond-centered Cayley tree into two equal halves at the central bond. Using the ground state, we compute the reduced density matrix ρ_{RDM} [see Eq. (3.1)] of one of the halves and diagonalize it. The corresponding eigenvalues are arranged by total S_z and the resultant plot is the "entanglement spectrum." Appropriate cuts are also chosen for the site-centered and Fibonacci trees as shown in Fig. 10.

The entanglement spectrum shows a copy of the largest eigenvalue in every S_z sector ranging from $-I_b$ to $+I_b$, where I_b is the net sublattice imbalance and is given by $(2^g \pm 1)/6$ as mentioned in Eq. (2.3). This indicates the presence of a "giant spin" of spin length I_b whose multiplet is given by the eigenvectors corresponding to these large eigenvalues. Given this picture, we explain the existence of the "anomalous" scale of energies.

1. *Bond-centered tree*

The Heisenberg Hamiltonian on the bond-centered Cayley tree may be rewritten as

$$H = H_{\text{left}} + H_{\text{right}} + J\mathbf{S}_0 \cdot \mathbf{S}_1. \tag{5.16}$$

where 0 and 1 refer to the central two sites of the tree (as has been schematically represented in Fig. 11). We treat the term corresponding to the central bond $J\mathbf{S}_0 \cdot \mathbf{S}_1$ as a perturbation within degenerate first order perturbation theory. The many-body ground state on each half is a degenerate multiplet of spin I_b. Since all spins on the left and right contribute in a definite proportion to the "giant spin" operators $\mathbf{T}_L$ and $\mathbf{T}_R$, one can reexpress the expectation values of the $J\mathbf{S}_0 \cdot \mathbf{S}_1$ in terms of $\mathbf{T}_L$ and $\mathbf{T}_R$. Note that expectation values of the term $J\mathbf{S}_0 \cdot \mathbf{S}_1$ are computed in the product basis of the two systems given by $|T_L, T_L^z\rangle \otimes |T_R, T_R^z\rangle$.

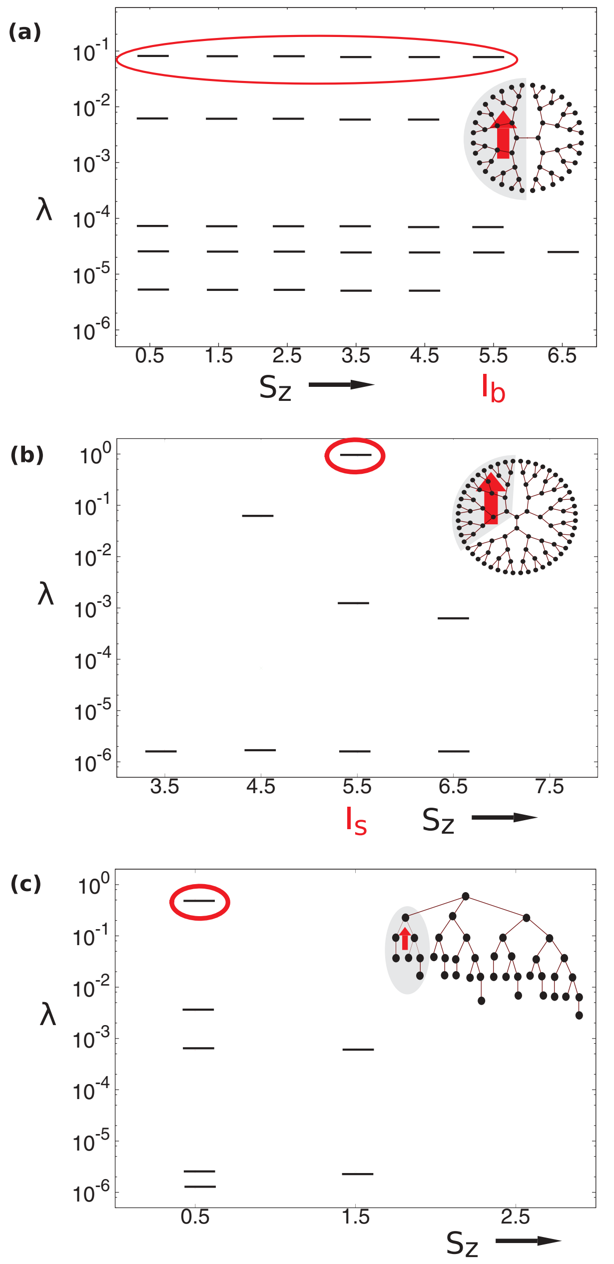

FIG. 10. (Color online) The entanglement spectrum for the bond-centered, site-centered, and Fibonacci trees as shown in the inset. λ refers to the eigenvalue of the reduced density matrix of the shaded area. The ground state for the bond-centered and Fibonacci clusters was a singlet and only the $S_z > 0$ sectors are shown. For the site-centered cluster we chose to work with the maximal S_z sector (which is the $S_z = 16$ for the 94-site cluster). I_b and I_s denote the "imbalance" metric defined in the introduction [refer to Eq. (2.3)]. For the bond-centered case, the largest degenerate eigenvalues of the reduced density matrix indicate a multiplet whose spin length exactly equals the imbalance I_b. For the site-centered case, the density matrix has largest weight in a state whose spin is I_s. For the Fibonacci case, a spin-1/2 state has the largest weight in the density matrix.

If all the spins in one half of the cluster had equal participation in their collective multiplet (observed in the entanglement spectrum), then

$$\langle T_L, T_L^z | \mathbf{S}_o | T_L T_L^{'z} \rangle = -\langle T_L, T_L^z | \mathbf{S}_e | T_L T_L^{'z} \rangle, \tag{5.17}$$

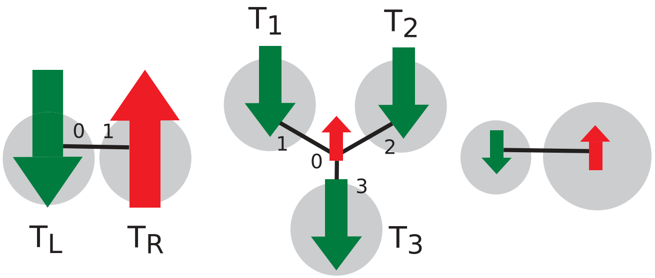

(a) Bond centered (b) Site centered (c) Fibonacci

FIG. 11. (Color online) Schematic of the "giant spins", which are the low-energy degrees of freedom for the bond- and site centered clusters (and which are absent for the Fibonacci tree).The numbering of sites shown here is used for the purpose of explaining our arguments in the text.

where e (o) refers to *any* even (odd) sublattice site in the same half of the bond-centered cluster. Therefore, if one were to create the equally weighted spin operator $\mathbf{T_L} = \sum_i \mathbf{S}_i$ and consider its matrix elements one would get

$$\langle \mathbf{T}_L \rangle = \pm 2 I_b \langle \mathbf{S}_0 \rangle , \tag{5.18}$$

where 0 refers to the central site in one half of the bond-centered cluster. The sign depends on whether the central site and the boundary sites are on the same (+) or opposite (−) sublattices.

What happens when the spins are not equally participating in the multiplet? The simplifying assumption we make here is that within the projected low-energy subspace, each individual spin-1/2 operator at lattice site i, $\mathbf{S}_i$, is proportional to the operator $\mathbf{T}_L/I_b$.

Using the fact that $I_b \sim N_s$, this relation can be expressed as

$$\mathbf{S}_0 = \frac{\gamma_b}{N_s} \mathbf{T}_L, \tag{5.19}$$

where the constant γ_b has been used to denote the proportionality factor. A similar relation exists for $\mathbf{S}_1$ and $\mathbf{T}_R$. From Eq. (5.19) it follows that

$$J \langle \mathbf{S}_0 \cdot \mathbf{S}_1 \rangle = \frac{J\gamma_b^2}{N_s^2} \langle \mathbf{T}_L \cdot \mathbf{T}_R \rangle . \tag{5.20}$$

The Hamiltonian $\mathbf{T}_L \cdot \mathbf{T}_R$ is diagonalized by coupling the left and right "giant spins" into a spin for the whole system, i.e., $\mathbf{T} = \mathbf{T}_L + \mathbf{T}_R$, whose eigenstates are given by $|T, T^z\rangle$:

$$\langle \mathbf{T}_L \cdot \mathbf{T}_R \rangle_{|T,T^z\rangle} = \tfrac{1}{2} \langle \mathbf{T}^2 - \mathbf{T}_L^2 - \mathbf{T}_R^2 \rangle \tag{5.21}$$

$$= \tfrac{1}{2} T(T+1) - I_b(I_b+1), \tag{5.22}$$

where T varies from $0,1.....,2I_b$. Note that T_L and T_R are constant and equal to I_b. The term $I_b(I_b+1)$ is a harmless constant energy shift to all states. Thus, the energy spectrum (up to a overall shift) as a function of T is simply

$$E(T) = \frac{J\gamma_b^2}{2N_s^2} T(T+1). \tag{5.23}$$

This is exactly the Hamiltonian of a quantum rotor with an "anomalous" moment of inertia scaling as N_s^2. This simple picture, hence, rather remarkably explains our numerical observations in Sec. IV B. We find γ_b to be $\sim$3.24 from fits to our numerical data based on finite-size scaling of the moment of inertia.

Note that though the giant spins are interacting via a weak bond, the fact that they are paired up in a singlet ground state makes the state highly entangled. In comparison, as we shall soon see, the ground state of the site-centered tree (in the $S_z = S_0$ sector) is closer to a product state of the giant spins and hence has a lower degree of entanglement. (This also explains why the convergence of DMRG calculations is more rapid with the number of states M for the site-centered case as compared to the bond-centered case.)

2. *Site-centered tree*

Let us now perform essentially the same analysis for the site-centered Cayley tree to further shed light on (and validate) the "giant spins" picture. Rewriting the Heisenberg Hamiltonian we get,

$$H = H_1 + H_2 + H_3 + J\mathbf{S}_0 \cdot (\mathbf{S}_1 + \mathbf{S}_2 + \mathbf{S}_3)\,. \tag{5.24}$$

where 0 refers to the central site and 1, 2, 3 refer to the sites connected to it (as has been schematically represented in Fig. 11). As before, make the substitution of $\mathbf{S}_1$, $\mathbf{S}_2$, $\mathbf{S}_3$ in terms of the giant spins $\mathbf{T}_1$, $\mathbf{T}_2$, $\mathbf{T}_3$ each of which has spin length I_s. Then couple the three giant spins into a bigger giant spin $\mathbf{T}$. The Hamiltonian now reads as

$$H = H_1 + H_2 + H_3 + \frac{J\gamma_s}{N_s}\mathbf{S}_0 \cdot \mathbf{T}, \tag{5.25}$$

where γ_s is a constant and $\mathbf{T} = \mathbf{T}_1 + \mathbf{T}_2 + \mathbf{T}_3$. Note that the angular momentum coupling rules predict that the value of T is in the range from 0, 1, ..., to $3I_s$.

Let us now couple the giant spin $\mathbf{T}$ to the spin-1/2 degree of freedom at the center of the cluster. The energy (in units of $J\gamma_s/N_s$ and up to a constant of $-\frac{3}{4}$) for the $S = 3I_s + \frac{1}{2}$ and $3I_s - \frac{1}{2}$ states is given by

$$E^{3I_s+\frac{1}{2}}_{3I_s} = \left(3I_s + \frac{1}{2}\right)\left(3I_s + \frac{3}{2}\right) - 3I_s\,(3I_s + 1)\,, \tag{5.26a}$$

$$E^{3I_s-\frac{1}{2}}_{3I_s} = \left(3I_s - \frac{1}{2}\right)\left(3I_s + \frac{1}{2}\right) - 3I_s\,(3I_s + 1)\,, \tag{5.26b}$$

where the superscript indicates the global value of the spin S and the subscript is used to indicate the T value it was made of. Similarly we have

$$E^{3I_s-\frac{1}{2}}_{3I_s-1} = \left(3I_s - \frac{1}{2}\right)\left(3I_s + \frac{1}{2}\right) - 3I_s\,(3I_s - 1)\,, \tag{5.27a}$$

$$E^{3I_s-\frac{3}{2}}_{3I_s-1} = \left(3I_s - \frac{3}{2}\right)\left(3I_s - \frac{1}{2}\right) - 3I_s\,(3I_s - 1)\,. \tag{5.27b}$$

Simplifying equations and incorporating the constant of $-\frac{3}{4}$, we get

$$E^{3I_s+\frac{1}{2}}_{3I_s} = 3I_s, \tag{5.28a}$$

$$E^{3I_s-\frac{1}{2}}_{3I_s} = -3I_s - 1, \tag{5.28b}$$

$$E^{3I_s-\frac{1}{2}}_{3I_s-1} = 3I_s - 1, \tag{5.28c}$$

$$E^{3I_s-\frac{3}{2}}_{3I_s-1} = -3I_s. \tag{5.28d}$$

Observe that $E^{3I_s-\frac{1}{2}}_{3I_s}$ is the lowest energy. This is in concordance with the Lieb-Mattis theorem;[32] i.e., the ground state has total spin $S_0 = 3I_s - \frac{1}{2}$. The energy gap (now in absolute units) of the S_0 to $S_0 + 1$ transition is given by

$$\Delta\,(S_0 \rightarrow S_0 + 1) = \frac{J\gamma_s}{N_s}\,(6I_s + 1)\,. \tag{5.29}$$

Since I_s is approximately $N_s/18$ for large N_s we get a gap of

$$\Delta\,(S_0 \rightarrow S_0 + 1) \approx \frac{J\gamma_s}{3}. \tag{5.30}$$

This is consistent with our numerical observation that the gap is finite in the large-N_s limit. Since the measured gap is $\sim 0.73J$ we infer that γ must be $\sim$2.19.

We give further credibility to our giant spin interpretation by testing the prediction of the gap for the S_0 to $S_0 - 1$ transition. This turns out to be gapless in the large-N_s limit,

$$\Delta\,(S_0 \rightarrow S_0 - 1) \approx \frac{J\gamma_s}{N_s}, \tag{5.31}$$

which is consistent with our DMRG calculations The measured γ_s from the fit of the DMRG data to $\Delta = J\gamma_s/N_s$ is found to be $\sim$2.19, consistent with the estimate from Eq. (5.30), serving as another check of the theory.

3. *Fibonacci Cayley tree*

The entanglement spectrum of the Fibonacci Cayley tree [see Fig. 10(c)] indicates the creation of a spin-1/2 degree of freedom as opposed to the "giant spins" encountered previously. The cut shown in Fig. 10(c) shows a region having an imbalance of one, which is the maximum possible for any cut.

We believe the lowest energy excitation of this system involves a breaking of a dimer and creation of two unpaired spins. Since the bonds in the interior have a decreasing dimerization strength, the energy required to create this excitation is expected to be vanishingly small in the infinite-lattice limit. This is seen in the spin gap in Table IV, but an explanation of the observed numerical exponent is a subject of further investigation and beyond the scope of this paper.

VI. SCHWINGER-BOSON MEAN-FIELD THEORY FOR SINGLET GROUND STATES

Can we understand the presence or absence of long-range order on these trees at the mean-field level? For this we appeal to the Schwinger-boson mean-field theory[5] which is capable of describing quantum disordered and ordered states within the same framework.[4,41] In this section we will see that this theory is a good description of the singlet ground states of the bond-centered and Fibonacci trees. This section also serves to expand the domain of application of the Schwinger-boson formalism to situations where multiple parameters need to be optimized simultaneously[42] (such as nonuniform systems or systems with very few symmetries).

A. Notation and formal setup

The $SU(N)$ Heisenberg Hamiltonian is expressed in terms of Schwinger bosons by defining a bond operator

$$\mathcal{A}_{ij} = \sum_{m=1}^{N} b_{im} b_{jm}, \tag{6.1}$$

where each Schwinger-boson operator b_{im} carries two labels i or j for site indices and m for flavor index. The physical Heisenberg model Eq. (2.1) corresponds to $N = 2$. The procedure is to decouple the quartic bosonic Hamiltonian into a one-body mean-field Hamiltonian by doing an expansion in $1/N$. Solving the mean-field Hamiltonian and putting in $N = 2$ allows us to compare the SBMFT results with DMRG calculations.

The $SU(N)$ Hamiltonian in terms of Schwinger bosons is

$$\mathcal{H}_{Heis} = -\frac{J}{N} \sum_{\langle ij \rangle} (\mathcal{A}_{ij}^{\dagger} \mathcal{A}_{ij} - 2S^2). \tag{6.2}$$

The mapping of the spin Hamiltonian to Schwinger bosons is exact if we meet the condition site by site,

$$\sum_{m=1}^{N} b_{im}^{\dagger} b_{im} = NS, \tag{6.3}$$

which ensures that the Hilbert space of the bosons is restricted by the spin size S (and the corresponding $|S,S_z\rangle$ states). However, we will impose this constraint only on the expectation $b_{im}^{\dagger} b_{im} \rightarrow \langle b_{im}^{\dagger} b_{im} \rangle_{MF}$. As a result of not satisfying Eq. (6.3) exactly, the mean-field energy E_{MF} and correlations differ from exact results (DMRG calculations) by overall scale factors.[5,43]

The decoupled mean field Hamiltonian $\mathcal{H}_{MF}$ is expressed in terms of the following variational parameters: a set of bond variables Q_{ij} for every bond i,j, Lagrange multipliers λ_i which impose Eq. (6.3), and a condensate field $\beta_i = \delta_{1,m} \langle b_{im} \rangle / \sqrt{N}$ which develops a nonzero value in a phase with LRO.[41] $\mathcal{H}_{MF}$ is then given by[6]

$$\mathcal{H}_{MF} = \sum_{i=1}^{N_s} \lambda_i \left(\sum_{m=1}^{N} b_{im}^{\dagger} b_{im} - NS \right) + \frac{N}{J} \sum_{\langle ij \rangle} |Q_{ij}|^2 + \sum_{i<j} (Q_{ij} \mathcal{A}_{ij}^{\dagger} + Q_{ij}^{*} \mathcal{A}_{ij}) + \frac{1}{\sqrt{N}} \sum_{i=1}^{N_s} (\phi_i^{*} b_{i1} + \phi_i b_{i1}^{\dagger}). \tag{6.4}$$

The field ϕ_i couples linearly to Schwinger bosons and is conjugate to $\delta_{1,m} \langle b_{im}^{\dagger} \rangle$. As a result of this parametrization, the lowest spinon frequency mode ω_0 of the $m = 1$ flavor develops a macroscopic occupation of Schwinger bosons on Bose condensation. At the mean-field level the different boson flavors decouple and the part of the mean-field Hamiltonian quadratic in bosonic operators $b_{im}, b_{im}^{\dagger}$ $(m = 2,\ldots,N)$ can be expressed as $N - 1$ copies of a quadratic Hamiltonian $\mathcal{H}_{MF}^{m}$. $\mathcal{H}_{MF}^{m}$ is given by

$$\mathcal{H}_{MF}^{m} = \sum_{i=1}^{N_s} \lambda_i b_{im}^{\dagger} b_{im} + \sum_{i<j} (Q_{ij} b_{im}^{\dagger} b_{jm}^{\dagger} + \text{H.c.}). \tag{6.5}$$

Integrating out the bosonic fields then gives us a set of single-spinon frequency modes and the total mean-field energy E_{MF}. Since we do not have the luxury of momentum space, we adopt a real-space Bogoliubov diagonalization procedure.[44] Since $\mathcal{H}_{MF}^{m}$ is block diagonal in the flavor basis (the Hamiltonian is the same for all $N - 1$ flavors) we can now drop the flavor index m and express it as

$$\mathcal{H}_{MF}^{m} = \frac{1}{2} (\mathbf{b}^{\dagger} \quad \mathbf{b}) \begin{pmatrix} \mathbf{\Lambda} & \boldsymbol{Q} \\ \boldsymbol{Q} & \mathbf{\Lambda} \end{pmatrix} \begin{pmatrix} \mathbf{b} \\ \mathbf{b}^{\dagger} \end{pmatrix}, \tag{6.6}$$

where $m \neq 1$, $\mathbf{b} = (b_1, b_2, \ldots, b_{N_s})$, and $\mathbf{\Lambda}$ and $\boldsymbol{Q}$ are $N_s \times N_s$ matrices given by $\mathbf{\Lambda}_{ij} = \lambda_i \delta_{ij}$ and $\boldsymbol{Q}_{ij} = Q_{ij}$ for nearest neighbor sites i,j. $\mathcal{H}_{MF}^{m}$ can now be diagonalized by introducing Bogoliubov transfomation matrices $\mathbf{U}$ and $\mathbf{V}$ defined as follows:

$$\begin{pmatrix} \mathbf{b} \\ \mathbf{b}^{\dagger} \end{pmatrix} = \begin{pmatrix} \mathbf{U} & \mathbf{V} \\ \mathbf{V}^{*} & \mathbf{U}^{*} \end{pmatrix} \begin{pmatrix} \boldsymbol{\alpha} \\ \boldsymbol{\alpha}^{\dagger} \end{pmatrix}, \tag{6.7}$$

where $\boldsymbol{\alpha} = (\alpha_1, \alpha_2, \ldots, \alpha_{N_s})$ is a vector of Bogoliubov quasiparticle annihilation operators. Each quasiparticle creation (annihilation) operator $\alpha_{\mu}^{\dagger}$ (α_{μ}) creates (destroys) a bosonic quasiparticle in the single-particle mode μ, where μ goes from 1 to N_s. The transformation (6.7) allows us to switch to the Bogoliubov quasiparticle basis where $\mathcal{H}_{MF}^{m}$ becomes

$$\mathcal{H}_{MF}^{m} = \sum_{\mu=1}^{N_s} \omega_{\mu} \left(\alpha_{\mu}^{\dagger} \alpha_{\mu} + \frac{1}{2} \right). \tag{6.8}$$

We can now perform a Legendre transformation to replace the field ϕ_i by β_i, allowing us to express E_{MF} as

$$\frac{E_{MF}}{N} = \sum_{\mu=1}^{N_s} \frac{1}{2} \omega_{\mu_i} + \frac{1}{J} \sum_{i>j} |Q_{ij}|^2 - \left(S + \frac{1}{2} \right) \sum_{i=1}^{N_s} \lambda_i + E_{\text{cond}}, \tag{6.9}$$

and E_{cond} is given by

$$E_{\text{cond}} = \sum_{i=1}^{N_s} \lambda_i |\beta_i|^2 + \sum_{i<j} (Q_{ij} \beta_i^{*} \beta_j^{*} + \text{H.c.}). \tag{6.10}$$

We now consider the case of $N = 2$. The variational parameters $\{\lambda_i\}, \{Q_{ij}\}$, and $\{\beta_i\}$ are determined by minimizing E_{MF} with respect to each of them giving the following constraints:

$$\frac{\partial E_{MF}}{\partial \lambda_i} = 0 \Rightarrow |\beta_i|^2 + \langle b_{i2}^{\dagger} b_{i2} \rangle = S, \tag{6.11a}$$

$$\frac{\partial E_{MF}}{\partial Q_{ij}} = 0 \Rightarrow \beta_i^{*} \beta_j^{*} + \frac{\langle \mathcal{A}_{ij} \rangle}{N} + \frac{1}{J} Q_{ij} = 0, \tag{6.11b}$$

$$\frac{\partial E_{MF}}{\partial \beta_i} = 0 \Rightarrow \lambda_i \beta_i^{*} + \sum_{j \text{ nn} i} Q_{ij}^{*} \beta_j^{*} = 0. \tag{6.11c}$$

One of the obvious considerations of applying this theory to such a nonuniform lattice is the large number of variational parameters which, in general, scale with the system size N_s. However, due to the symmetries of the Cayley tree the number of independent parameters are reduced to order g. The task then is to find an optimal set of parameters $\{\lambda_i^{*}, Q_{ij}^{*}, \beta_i^{*}\}$ which satisfy the constraints in (6.11a), (6.11b), and (6.11c).

This is done numerically and is discussed in Sec. VI C. The resulting optimal $E_{MF}(\lambda_i^*, Q_{ij}^*, \beta_i^*)$ can be related to the physical Heisenberg energy via

$$E_{\text{Heis}} = 2E_{MF} + \sum_{\langle ij \rangle} J S^2. \tag{6.12}$$

A note on the β_i minimization constraint (6.11c): A trivial solution of this equation is to choose $\beta_i = 0$ for all sites. This is the quantum disordered phase. A nonzero value of β_i signals condensation of Schwinger bosons and long-range order.

For finite uniform systems there is no spontaneous symmetry breaking and correspondingly no condensation of bosons.[45] Introduction of the condensate field β_i is analogous to applying a staggered field in the system that couples to the staggered magnetization. This breaks the degeneracy of the single-particle energies corresponding to the two boson flavors (for $N = 2$). The condensate fraction begins to build up in the flavor mode with the lowest frequency.

The algorithm tries to initially find a self-consistent mean-field solution by varying only the set of λ_i and Q_{ij}'s. However, if we cannot satisfy the constraints in Eqs. (6.11a) and (6.11b) (with $\beta_i = 0$), we resort to adding the condensate field β_i, as an additional set of variational parameters. While we cannot completely rule out the possibility of a solution with $\beta_i = 0$, we believe that the appearance of a condensate is *physical*.

B. Correlation functions in quantum disordered and LRO phase

Here we compute correlation functions that enter into the self-consistency equations (6.11a), (6.11b), and (6.11c). The boson density of a given flavor at site i is given by (suppressing the flavor index)

$$\begin{aligned} \langle b_i^\dagger b_i \rangle &= \sum_{p,q=1}^{N_s} \langle \left(\mathbf{U}_{ip}^* \boldsymbol{\alpha}_p^\dagger + \mathbf{V}_{ip}^* \boldsymbol{\alpha}_p \right) \left(\mathbf{U}_{iq} \boldsymbol{\alpha}_q + \mathbf{V}_{iq} \boldsymbol{\alpha}_q^\dagger \right) \rangle \\ &= \sum_{p,q=1}^{N_s} \mathbf{V}_{ip}^* \mathbf{V}_{iq} \langle \boldsymbol{\alpha}_p \boldsymbol{\alpha}_q^\dagger \rangle \\ &= \left(\mathbf{V}^* \mathbf{V}^T \right)_{ii}. \end{aligned} \tag{6.13}$$

The indices p,q run over all single-particle modes and we made use of $\langle \boldsymbol{\alpha}_p \boldsymbol{\alpha}_q^\dagger \rangle = \delta_{p,q}$ which follows since the SBMFT many-body ground state is the vacuum of Bogoliubov quasiparticles. Similarly,

$$\langle b_i b_j \rangle = (\mathbf{U}\mathbf{V}^T)_{ij}. \tag{6.14}$$

Spin correlation functions G_{ij} can be computed in a similar fashion. The only complication arises in the $SU(2)$ broken-symmetry phase where, due to loss of spin rotational invariance, we need to compute the $\langle S_i^z S_j^z \rangle$ correlations. This involves evaluating a quartic expectation which we decouple into a series of 2-point functions using Wick's theorem. For simplicity of notation we define the following combinations of $\mathbf{U}$ and $\mathbf{V}$ matrices:

$$\begin{aligned} \tilde{\mathbf{Q}} &\equiv \mathbf{U}\mathbf{V}^T, \\ \tilde{\mathbf{U}} &\equiv \mathbf{U}\mathbf{U}^\dagger, \\ \tilde{\mathbf{V}} &\equiv \mathbf{V}\mathbf{V}^T. \end{aligned} \tag{6.15}$$

Spin correlations in the quantum disordered and the broken-symmetry LRO phase are then given by

$$(G_{ij})_{Q.dis.} = \begin{cases} -\frac{3}{2} \tilde{\mathbf{Q}}_{ij}^\dagger \tilde{\mathbf{Q}}_{ij} \\ \text{for } i \in A, j \in B, \\ \frac{3}{2} \tilde{\mathbf{V}}_{ij} \tilde{\mathbf{U}}_{ij} \\ \text{for } (i,j) \in A \text{ or } B, \end{cases} \tag{6.16a}$$

$$(G_{ij})_{LRO} = \begin{cases} -N\beta_i\beta_j \tilde{\mathbf{Q}}_{ij} - \frac{1}{4} \tilde{\mathbf{Q}}_{ij}^\dagger \tilde{\mathbf{Q}}_{ij} \\ \text{for } i \in A, j \in B, \\ \frac{1}{2} N\beta_i\beta_j \left(\tilde{\mathbf{U}} + \tilde{\mathbf{V}} \right)_{ij} + \frac{1}{4} \tilde{\mathbf{V}}_{ij} \tilde{\mathbf{U}}_{ij} \\ \text{for } (i,j) \in A \text{ or } B. \end{cases} \tag{6.16b}$$

In the quantum disordered phase SBMFT overestimates G_{ij} by an overall scale factor[5] of $3/2$. We normalize the SBMFT correlation function by this factor to take into account the $1/N$ fluctuation effects for $N = 2$. Similarly, in the phase with LRO we find that we need to scale up G_{ij} by a factor of 1.8 to make it agree quantitatively with DMRG results. Similar overall scale factors have been reported previously.[43] These overall scale factors can be suppressed by using Gutzwiller projected mean field wave functions,[46] which is feasible only for small system sizes. Such projected wave functions have also been shown to give energies in agreement with exact results.[43,46]

C. Numerical implementation

Using the symmetry of the bond-centered Cayley tree, we reduce the number of variational mean field parameters. A first simplification results from the fact that all sites within a given shell on the lattice are equivalent and are therefore assigned the same λ_i and β_i. Similarly, all bonds connecting two successive shells are equivalent and have the same Q_{ij}'s. For the Fibonacci cluster there are fewer exact symmetries (only reflection about the central bond) compared to the Cayley tree and therefore a larger number of variational parameters are required.

We use the Nelder-Mead simplex optimizer from the GSL library to minimize the following weighted combined cost function which aims to reduce (6.9) subject to the constraints (6.11a), (6.11b), and (6.11c). Since each of these constraint equations are obtained by minimizing (6.9) with respect to the variational parameters λ_i, Q_{ij}, and β_i, enforcing the constraints will minimize E_{MF}:

$$C(\{\lambda_i\},\{Q_{ij}\},\{\beta_i\}) = \mu_0 C_\lambda + \mu_1 C_Q + \mu_2 C_\beta, \tag{6.17}$$

where $\{\mu_0,\mu_1,\mu_2\}$ are relative weights of terms in the cost function and the costs are given by

$$C_\lambda = \sum_{i=1}^{N_s} [(|\beta_i|^2 + \langle b_{i2}^\dagger b_{i2} \rangle) - S]^2, \tag{6.18a}$$

$$C_Q = \sum_{i<j} \left(\beta_i \beta_j + \frac{1}{N} \langle \mathcal{A}_{ij} \rangle + \frac{1}{J} Q_{ij} \right)^2, \tag{6.18b}$$

$$C_\beta = \sum_{i=1}^{N_s} \left(\lambda_i \beta_i^* + \sum_{j \text{nn} i} Q_{ij}^* \beta_j^* \right)^2. \tag{6.18c}$$

In practice, to minimize the weighted cost function (6.17), tolerance values for the C_β and C_λ are set at 10^{-8} and 10^{-14} respectively and the Q_{ij}'s are solved for self-consistently. A good initial guess for the Q_{ij}'s is a pattern that favors dimerization as suggested by results from exact diagonalization for small clusters. A good rule of thumb for the bond-centered cluster is to begin by dimerizing (assigning a high value of Q_{ij}) the outermost bond and to create a pattern, moving inwards, of alternating bond strengths.

For cases requiring a larger number of variational parameters (like in the case of the Fibonacci cluster) it helps to guide the Nelder-Mead optimization using a "relaxation" algorithm. The algorithm starts with an initial guess for the Q_{ij}'s and allows the optimizer to find an optimal set of λ_i's. If the tolerance level for C_λ is not met, the Q_{ij}'s are allowed to relax; i.e., the best set of λ_i's is taken as an initial guess in an optimization where the Q_{ij}'s are now taken to be the variational parameters. Thus, by alternating in the choice of variational parameters between the λ_i and the Q_{ij} for each optimization cycle we converge to the desired tolerance limit.

The stability of the obtained mean-field solution was checked by adding small random perturbations to the optimal mean-field parameters. In the quantum disordered phase, the saddle point was checked to correspond to a maximum in the λ_i and a minimum in the Q_{ij}.

Every optimization cycle scales as $\sim N_s^3 \tau$, where τ is the total time for functional evaluation taken by the optimizer to converge to a solution. A typical optimization time for the $N_s = 126$ cluster is about 20 minutes on a personal workstation (2.7 GHz Intel Core i7).

D. Results

The landscape of the cost function (6.17) in parameter space has many local minima with very similar mean-field energies (differing by 1% or less). As a result, we get a zoo of physically plausible mean-field solutions, all of which satisfy (6.11a) and have comparable E_{MF}. To choose the optimal solution from among these, we look at the β_i minimization constraint (6.11c) and hand pick the one which has the lowest C_β. In other words, the chosen solution has the lowest spinon frequency ω_0.

The mean-field energy and correlation functions for the bond-centered Cayley trees suffer from significant finite-size effects (number of sites on the boundary scales as the system size N_s). As a result, for the finite systems considered above, the lowest spinon frequency is always gapped $\omega_0 \neq 0$ in spite of a very low β_{cost} ($\sim 10^{-8}$). However, with increasing system size, ω_0 lowers and spinons begin to condense in this lowest frequency mode. A good (to within 5%) fit to the lowest spinon frequency versus system size N_s plot is given by the function $\omega_0(N_s) = 0.067/N_s + 1.626/N_s^2$. Spinon condensation and a very small ω_0 suggest long-range order in the thermodynamic limit.

Since condensation of spinons signals long-range order, sites with a higher condensate fraction have a greater participation in establishing Néel order on the cluster. By mapping out the condensate fraction on different radial shells in Fig. 12(b) we notice the strong correspondence between sites with large condensate densities and those with a high "flippability" as in Eq. (5.8).

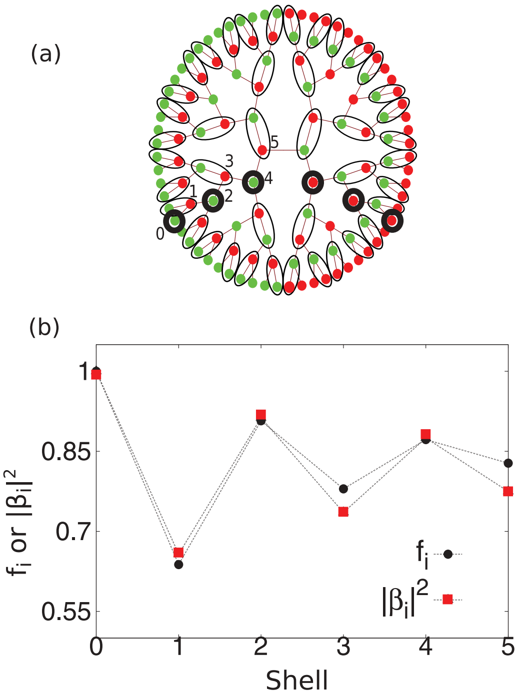

FIG. 12. (Color online) (a) Heuristic for computing the number of "dangling spins" as proposed by Wang and Sandvik. (b) The magnitude of the "flippability" as in Eq. (5.8) computed from DMRG and the condensate fraction $|\beta_i|^2$ computed from SBMFT on every shell of the bond-centered Cayley tree. Both quantities are qualitatively consistent with each other and confirm the "dangling" spin heuristic shown above.

Our results can be put in perspective with respect to a heuristic for computing the number of "dangling spins" proposed by Wang and Sandvik[19] who encountered the role of sublattice imbalance in the context of percolation clusters on the square lattice. In their picture, geometric constraints of a diluted square lattice forbid spins from pairing up with their neighbors into dimers, leaving some of them unpaired or "dangling."[19] They believed these emergent spins to be the effective low-energy degrees of freedom. In a similar spirit we "dimerize" the lattice maximally as shown in Fig. 12(a) and the spins that remain are called "dangling." These are the representative spins participating as the low-energy degrees of freedom. (Note that the choice of maximal dimer covering is not unique but the number of uncovered spins is the same in all such coverings.)

VII. CONCLUSION

In this paper, we have explored the relationship between sublattice imbalance and nature of the low-energy spectrum of the bond-centered, site-centered, and Fibonacci Cayley trees. For the bond-centered Cayley tree, we find that the spin gap scales with size as $1/N_s^\alpha$ where α was found to be ≈ 2. We discover an entire tower of states (Fig. 6) with a much larger moment of inertia (Sec. IV B) than the Anderson tower of states. This low-energy scale persists up to a spin value of $S^* = 2I_b$, where I_b refers to a measure of the imbalance (or the number of "unpaired spins") on the bond-centered tree [as in Eq. (2.3)].

To highlight the role of sublattice imbalance, we introduced the Fibonacci Cayley tree in Sec. II, which does not have any locally unpaired spins. We found it lacks the low-lying states characteristic of the bond-centered tree (see Fig. 6). Instead, the spin gap vanishes as $\approx 1/N_s^{0.6}$. However, both trees have similar susceptibilities ($\sim N_s$) at sufficiently large magnetic fields. This is because the strength of the dimerization is relatively weak at sufficiently high energy scales (comparable to J), allowing all spins to lock together, leading to an extensive susceptibility.

For the site-centered tree, our results are in good agreement with a recent study.[22] We report a finite spin gap of $\Delta = 0.731(4)$ in the infinite-lattice limit and a ground-state energy of $e_0 = -0.393854(1)$.

Our results can be explained within a unifying framework of individual spins coupling together to form collective spin degrees of freedom which we refer to as "giant spins." The idea for coupling big sublattice spins is well known[15] in the context of regular lattices. However, we emphasize that the "giant spins" are created by coupling all spins (both even and odd sublattice spins) in regions with large local sublattice imbalances. For the bond- and site-centered lattices, we find that all lattice sites have a (nearly) uniform participation in the "giant spins." This picture is developed in Sec. V using the single-mode approximation for the excited (triplet) state and observing the entanglement spectrum.

In a broader context, our study aims to understand the nature of unpaired spins coupling in a strongly dimerized background. Such spins, termed as "dangling spins," have been predicted from numerical simulations[19] for systems with quenched random dilution. Thus, a natural extension of our study is to consider such dangling spins on percolation clusters where we expect that they couple hierarchically to form emergent giant spins at different length scales. This will be the subject of a future publication.[36]

In this paper, we have explored several techniques to develop our understanding. To begin with, we obtain accurate many-body wave functions and their expectations using an implementation of the density matrix renormalization group (DMRG) procedure (described in Sec. III) that works for generic trees. In general, this procedure is expected to be well suited to hierarchical lattices and those with few or no loops, such as the Husimi cactus,[47,48] a lattice of corner-sharing triangles (whose centers form the vertices of the Cayley tree), and which is locally like the kagome lattice.

To have an understanding at the mean-field level, we adapted Schwinger-boson mean-field theory (SBMFT) to a larger number of variational parameters than considered previously.[43,46,49] We were able to study spin correlations of the bond-centered and Fibonacci trees (singlet ground states). Rather remarkably, the theory is quite accurate *quantitatively* in predicting ground-state spin-spin correlation functions (see Fig. 5), up to overall multiplicative scale factors (as discussed in Sec. VI). The recipe outlined in Sec. VI can be used to navigate through the zoo of feasible mean-field solutions by giving relative weights to the constraint equations (6.18a), (6.18b), and (6.18c).

We believe that most applications of SBMFT have focused on quantum disordered phases,[50,51] but the broken-symmetry phase has received less attention. The setup can also be generalized to handle frustrated spin systems without the need to have an ansatz for the mean-field fluxes or the decoupling parameters.[50] This might lead to novel spin liquid ground states with new kinds of broken symmetries.[42]

Recently we came across results by Misguich,[42] who has done an extensive numerical study of SBMFT formalism for spatially inhomogeneous states, mostly concentrating on gapped systems. However, his study differs from ours in that we include the condensate field as a variational parameter. It will be interesting to apply our formalism to further investigate his proposed set of ground states.

ACKNOWLEDGMENTS

H.J.C. would like to thank G. K. Chan and S. Sharma for discussions on the DMRG technique, N. Nakatani for numerical checks against his tree tensor network code, and C. J. Umrigar and the Cornell Physics Department for use of their computational facilities. We thank S. Pujari, L. Wang, S. Parameswaran, A. Sandvik, A. Auerbach, D. Arovas, and M. Lawler for discussions and J. Chalker for his suggestion to study the bond-centered Cayley tree. We also thank R. Lamberty for critically reviewing the manuscript. H.J.C., S.G., and C.L.H. acknowledge support from National Science Foundation Grant No. NSF DMR-1005466. This work made use of the Cornell Center for Materials Research computer facilities which are supported through the NSF MRSEC program (DMR-1120296).

APPENDIX A: DERIVATION OF THE SMA GAP EQUATION FOR THE HEISENBERG MODEL

In Sec. V, we introduced the single-mode approximation (SMA) for the excited state in terms of the ground state,

$$|1'\rangle = \sum_i u_i S_i^+ |0\rangle, \tag{A1}$$

where $|0\rangle$ is the singlet ground state and $|1'\rangle$ is the approximate triplet excited state. i refers to a site index. In this Appendix, we will derive an expression for the SMA energy gap Δ_{SMA} in terms of the ground-state correlations and the parameters u_i.

The expression for the gap between the ground and first excited state is

$$\Delta = \frac{\langle 1'|H|1'\rangle}{\langle 1'|1'\rangle} - E_0, \tag{A2}$$

where E_0 is the ground-state energy. Plugging in the expression for $|1'\rangle$ from Eq. (A1) we have

$$\Delta_{SMA} = \frac{\langle 0|\sum_{ij} u_i u_j S_j^- H S_i^+ |0\rangle}{\langle 0|\sum_{ij} u_i u_j S_j^- S_i^+ |0\rangle} - E_0 \tag{A3}$$

$$= \frac{\sum_{ij} u_i u_j \langle S_j^- [H, S_i^+]\rangle}{\sum_{ij} u_i u_j \langle S_j^- S_i^+\rangle} + \frac{\sum_{ij} u_i u_j \langle S_j^- S_i^+ H\rangle}{\sum_{ij} u_i u_j \langle S_j^- S_i^+\rangle} - E_0 \tag{A4}$$

$$= \frac{\sum_{ij} u_i u_j \langle S_j^- [H, S_i^+]\rangle}{2\sum_{ij} u_i u_j \langle S_j^z S_i^z\rangle}. \tag{A5}$$

Next, consider the nearest neighbor Heisenberg Hamiltonian,

$$H = \frac{J}{2} \sum_{\langle k,l \rangle} \left(S_k^z S_l^z + \tfrac{1}{2}(S_k^+ S_l^- + S_k^- S_l^+) \right), \tag{A6}$$

where $\langle k,l \rangle$ refer to nearest neighbor pairs. We have included a factor of 1/2 outside to compensate for counting each nearest neighbor term twice.

We now calculate $[H,S_i^+]$ occurring in Eq. (A5). To do so, we calculate $[\mathbf{S}_k \cdot \mathbf{S}_l, S_i^+]$ as

$$\begin{aligned} [\mathbf{S}_k \cdot \mathbf{S}_l, S_i^+] &= S_k^z [S_l^z, S_i^+] + S_l^z [S_k^z, S_i^+] + \\ &\quad \times \tfrac{1}{2} S_k^+ [S_l^-, S_i^+] + \tfrac{1}{2} [S_k^-, S_i^+] S_l^+ \\ &= \delta_{il} S_k^z S_l^+ + \delta_{ik} S_l^z S_k^+ \\ &\quad - \delta_{il} S_k^+ S_l^z - \delta_{ik} S_k^z S_l^+ . \end{aligned} \tag{A7}$$

The numerator of Eq. (A5) involves the term $\langle S_j^- [H,S_i^+] \rangle$. Hence we now consider the action of the S_j^- operator on the simplified expression for $[\mathbf{S}_k \cdot \mathbf{S}_l, S_i^+]$ in Eq. (A7). Consider only the terms that have $j = k$ or $j = l$ (since $k = l$ terms do not occur in the Hamiltonian we do not have to worry about the possibility $j = k = l$). In addition, time-reversal symmetry of the ground-state wave function (equivalent to simply asserting the $S_z \to -S_z$ symmetry of the ground state) ensures that if both $j \neq k$ and $j \neq l$ then the three-point correlation function is exactly 0. This latter point is rather subtle and so we expand on this in Appendix B.

Thus the expression for $S_j^- [\mathbf{S}_k \cdot \mathbf{S}_l, S_i^+]$ (after retaining only the $j = k$ and $j = l$ terms) is

$$\begin{aligned} &S_j^- [\mathbf{S}_k \cdot \mathbf{S}_l, S_i^+] \\ &= -\delta_{ik}\delta_{jl} \left(\frac{1}{2} - S_l^z \right) S_k^z - \delta_{ik}\delta_{jk} \frac{S_k^- S_l^+}{2} \\ &\quad - \delta_{il}\delta_{jk} \left(\frac{1}{2} - S_k^z \right) S_l^z - \delta_{il}\delta_{jl} \frac{S_l^- S_k^+}{2} + \delta_{jk}\delta_{il} \frac{S_k^- S_l^+}{2} \\ &\quad + \delta_{jl}\delta_{il} \left(\frac{1}{2} - S_l^z \right) S_k^z + \delta_{jk}\delta_{ik} \left(\frac{1}{2} - S_k^z \right) S_l^z \\ &\quad + \frac{1}{2} S_k^+ S_l^- \delta_{ik}\delta_{jl} . \end{aligned} \tag{A8}$$

Inserting (A8) into the expression for the SMA gap (A5) for the Heisenberg Hamiltonian and utilizing $\langle S_i^z \rangle = 0$ for all i, we obtain

$$\Delta_{SMA} = - \frac{\sum_{\langle k,l \rangle} (u_k - u_l)^2 \left\langle S_k^z S_l^z \right\rangle}{2 \sum_{ij} u_i u_j \left\langle S_i^z S_j^z \right\rangle} . \tag{A9}$$

APPENDIX B: WHY IS $\langle \psi | S_j^- S_k^+ S_l^z | \psi \rangle = 0$ FOR DISTINCT j,k,l?

To derive the SMA gap equation in Appendix A, we used

$$\langle \psi |\, S_j^- S_k^+ S_l^z \,| \psi \rangle = 0 \tag{B1}$$

for distinct site indices j,k,l. In this Appendix, we will prove this statement for *any* wave function which is invariant under time reversal.

Consider three distinct spins i,j,k. Express the wave function in the basis spanned by the three spins at sites j,k,l and the rest of the spins (collectively termed as "environment" e),

$$|\psi\rangle = \sum_{s_j' s_k' s_l'} \sum_{e} w_e^{s_j' s_k' s_l'} |s_j' s_k' s_l'\rangle \otimes |e\rangle . \tag{B2}$$

Since this wave function is an eigenstate of the Heisenberg model (with no external magnetic fields), it follows that under time reversal (denoted by operator T) we have

$$\psi \to z\psi , \tag{B3}$$

where z is ±1.

This implies that the coefficients in the wave function satisfy the relation

$$w_e^{s_j' s_k' s_l'} = z w_{-e}^{-s_j' - s_k' - s_l'} . \tag{B4}$$

The action of the operator $S_j^- S_k^+ S_l^z$ on $|\psi\rangle$ from Eq. (B2) yields

$$S_j^- S_k^+ S_l^z |\psi\rangle = \sum_{s_l'} \sum_{e} w_e^{\uparrow\downarrow s_l'} S_l' |\downarrow\uparrow s_l'\rangle \otimes |e\rangle . \tag{B5}$$

Now acting Eq. (B5) with $\langle \psi |$ from the left and using the orthogonality of the basis, we get

$$\langle \psi | S_j^- S_k^+ S_l^z | \psi \rangle = \sum_{s_l'} \sum_{e} w_e^{\downarrow\uparrow s_l'} w_e^{\uparrow\downarrow s_l'} S_l' \tag{B6}$$

$$\begin{aligned} &= \frac{1}{2} \sum_{e_-} w_{e_-}^{\downarrow\uparrow\uparrow} w_{e_-}^{\uparrow\downarrow\uparrow} \\ &\quad - \frac{1}{2} \sum_{e_+} w_{e_+}^{\downarrow\uparrow\downarrow} w_{e_+}^{\uparrow\downarrow\downarrow} , \end{aligned} \tag{B7}$$

where e_+ (e_-) reflects the fact that the environment carries a net S_z of $+(-)\frac{1}{2}$ since the wave function consists of $S_{\text{tot}}^z = 0$ terms only. Under inversion of all spins in e_+ we get e_-. With this in mind, consider the second sum on the right. Using the time-reversal symmetry of the wave function, i.e., $w_{e_+}^{\downarrow\uparrow\downarrow} = z w_{e_-}^{\uparrow\downarrow\uparrow}$ and $w_{e_+}^{\uparrow\downarrow\downarrow} = z w_{e_-}^{\downarrow\uparrow\uparrow}$ [as seen from Eq. (B4)], in Eq. (B7)

TABLE VI. Optimal SBMFT parameters for bond-centered clusters of various sizes.

N_s	Q_{ij}^*	λ_i^*	β_i^*	N_s	Q_{ij}^*	λ_i^*	β_i^*
14	0.672	1.639	0	126	– 0.568	1.893	0.43
	0.539	2.318	0		– 0.622	1.656	0.445
	0.676	0.523	0		– 0.579	2.026	0.392
30	0.561	1.921	0		– 0.622	1.497	0.42
	0.633	1.487	0		– 0.55	2.32	0.353
	0.543	2.345	0		– 0.677	0.546	0.443
	0.673	0.536	0	254	– 0.631	1.669	0.495
62	0.646	1.72	0		– 0.56	1.986	0.454
	0.57	1.975	0		– 0.622	1.537	0.504
	0.63	1.514	0		– 0.571	1.965	0.455
	0.551	2.345	0		– 0.622	1.495	0.497
	0.68	0.544	0		– 0.55	2.263	0.449
					– 0.671	0.563	0.56

we get

$$\langle\psi|S_j^- S_k^+ S_l^z|\psi\rangle = \frac{1}{2}\sum_{e_-} w_{e_-}^{\downarrow\uparrow\uparrow} w_{e_-}^{\uparrow\downarrow\uparrow} - \frac{1}{2}z^2\sum_{e_-} w_{e_-}^{\downarrow\uparrow\uparrow} w_{e_-}^{\uparrow\downarrow\uparrow} \tag{B8}$$

$$= 0, \tag{B9}$$

where we have used $z^2 = 1$.

APPENDIX C: SCHWINGER-BOSON MEAN-FIELD THEORY CALCULATIONS

As mentioned in Sec. VI, optimization of multiple parameters occurring in the Schwinger-boson theory for nonuniform systems was quite a challenging task. Hence, for interested readers, we report the exact values of the parameters obtained from our calculations, so that they may be able to reproduce our results.

The optimal mean-field parameters are tabulated in Table VI for different lattice sizes. In each column (from top to bottom) the parameters label inner to outermost most bonds/sites. The Q_{ij}'s alternate in strength across successive bonds consistent with the location of unpaired spins. Similar alternation in the condensate field β_i indicates the variation in the density of dangling spins across shells.

The ground-state energy from SBMFT for the 126-site cluster was found to be $\approx -0.533J$. This is lower than the DMRG estimate $-0.39385J$. This can be attributed to the well-known fact[45,49] about the nonvariational nature of SBMFT energies. This is because of not satisfying the constraints in Eq. (6.3) exactly.

---

[1] M. Takahashi, Prog. Theor. Phys. Suppl. **87**, 233 (1986); Phys. Rev. Lett. **58**, 168 (1987).

[2] J. E. Hirsch and S. Tang, Phys. Rev. B **40**, 4769 (1989).

[3] E. Manousakis, Rev. Mod. Phys. **63**, 1 (1991).

[4] S. Sarker, C. Jayaprakash, H. R. Krishnamurthy, and M. Ma, Phys. Rev. B **40**, 5028 (1989).

[5] A. Auerbach and D. P. Arovas, Phys. Rev. Lett. **61**, 617 (1988); D. P. Arovas and A. Auerbach, Phys. Rev. B **38**, 316 (1988).

[6] A. Auerbach and D. P. Arovas, arXiv:0809.4836.

[7] A. V. Chubukov, Phys. Rev. B **44**, 12318 (1991).

[8] A. V. Chubukov, S. Sachdev, and J. Ye, Phys. Rev. B **49**, 11919 (1994).

[9] N. Trivedi and D. M. Ceperley, Phys. Rev. B **41**, 4552 (1990).

[10] K. H. Hoglund and A. W. Sandvik, Phys. Rev. B **79**, 020405 (2009).

[11] M. A. Metlitski and S. Sachdev, Phys. Rev. B **78**, 174410 (2008).

[12] A. L. Chernyshev, Y. C. Chen, and A. H. Castro Neto, Phys. Rev. Lett. **87**, 067209 (2001).

[13] In the literature, the "Bethe lattice" is often used to refer to the thermodynamic limit of the "Cayley tree," where the effect of boundaries is eliminated [see for example Laumann *et al.* (Ref. 23) which considers random graphs of fixed connectivity]. For the purpose of this paper, the presence of open boundaries will play an important role in the low-energy physics and so we will simply use the term "Cayley tree."

[14] P. W. Anderson, Phys. Rev. **86**, 694 (1952); P. W. Anderson, *Basic Notions of Condensed Matter Physics* (Benjamin, New York, 1984), Sec. 2D, pp. 44-46.

[15] C. Lhuillier, arXiv:cond-mat/0502464.

[16] Subir Sachdev, *Quantum Phase Transitions* (Cambridge University Press, Cambridge, UK, 1999).

[17] H. Neuberger and T. Ziman, Phys. Rev. B **39**, 2608 (1989).

[18] M. Gross, E. Sanchez-Velasco, and E. Siggia, Phys. Rev. B **39**, 2484 (1989).

[19] L. Wang and A. W. Sandvik, Phys. Rev. Lett. **97**, 117204 (2006); Phys. Rev. B **81**, 054417 (2010).

[20] H. Otsuka, Phys. Rev. B **53**, 14004 (1996).

[21] B. Friedman, J. Phys.: Condens. Matter **9**, 9021 (1997).

[22] M. Kumar, S. Ramasesha, and Z. G. Soos, Phys. Rev. B **85**, 134415 (2012).

[23] C. R. Laumann, S. A. Parameswaran, and S. L. Sondhi, Phys. Rev. B **80**, 144415 (2009).

[24] G. Semerjian, M. Tarzia, and F. Zamponi, Phys. Rev. B **80**, 014524 (2009).

[25] W. F. Brinkman and T. M. Rice, Phys. Rev. B **2**, 1324 (1970).

[26] A. Georges, G. Kotliar, W. Krauth, and M. J. Rozenberg, Rev. Mod. Phys. **68**, 13 (1996).

[27] M. A. Martin-Delgado, J. Rodriguez-Laguna, and G. Sierra, Phys. Rev. B **65**, 155116 (2002).

[28] D. Astruc, E. Boisselier, and C. Ornelas, Chem. Rev. **110**, 1857 (2010).

[29] M. Takahata, M. Shoji, H. Nitta, R. Takeda, S. Yamanaka, M. Okumura, M. Nakano, and K. Yamaguchi, Int. J. Quantum Chem. **105**, 615 (2005).

[30] S. R. White, Phys. Rev. Lett. **69**, 2863 (1992); Phys. Rev. B **48**, 10345 (1993).

[31] W. Münder, A. Weichselbaum, A. Holzner, J. von Delft, and C. L. Henley, New J. Phys. **12**, 075027 (2010).

[32] W. Marshall, Proc. R. Soc. London A **232**, 48 (1955); E. H. Lieb and D. Mattis, J. Math. Phys. **3**, 749 (1962); M. B. Hastings, Phys. Rev. B **69**, 104431 (2004).

[33] K. G. Wilson, Rev. Mod. Phys. **47**, 773 (1975).

[34] M. B. Lepetit, M. Cousy, and G. M. Pastor, Eur. Phys. J. B **13**, 3 (2000).

[35] V. Murg, F. Verstraete, Ö. Legeza, R. M. Noack, Phys. Rev. B **82**, 205105 (2010).

[36] H. J. Changlani, S. Ghosh, S. Pujari, and C. L. Henley, arXiv:1210.4621.

[37] Z. Bai, J. Demmel, J. Dongarra, A. Ruhe, and H. van der Vorst (eds.), *Templates for the Solution of Algebraic Eigenvalue Problems: A Practical Guide* (SIAM, Philadelphia, PA, 2000).

[38] R. P. Feynman, *Statistical Mechanics* (Benjamin, New York, 1972).

[39] The expression $\sum_{k,l} u_k u_l G_{kl}$ is invariant under the transformation $u_i \to u_i + u$ though it is not manifestly evident at first glance. One can prove this by using two results specific to a singlet state. First,

$\sum_{ij} G_{ij} = S(S+1)$ which equals zero for a singlet state. Second, $\sum_{ij} u_j G_{ij} = \sum_j \langle S_z^{\mathrm{tot}} S_j^z \rangle$ which equals zero for a state with $S_z^{\mathrm{tot}} = 0$.

[40] C. R. Laumann, S. A. Parameswaran, S. L. Sondhi, and F. Zamponi, Phys. Rev. B **81**, 174204 (2010).

[41] S. Sachdev, Phys. Rev. B **45**, 12377 (1992).

[42] G. Misguich, Phys. Rev. B **86**, 245132 (2012).

[43] L. Messio, O. Cepas, and C. Lhuillier, Phys. Rev. B **81**, 064428 (2010).

[44] See, for example, E. R. Mucciolo, A. H. Castro Neto, and Claudio Chamon, Phys. Rev. B **69**, 214424 (2004).

[45] A. Auerbach, *Interacting Electrons and Quantum Magnetism* (Springer-Verlag, New York, NY, 1994).

[46] T. Tay and O. I. Motrunich, Phys. Rev. B **84**, 020404(R) (2011).

[47] P. Chandra and B. Doucot, J. Phys. A **27**, 1541 (1994).

[48] H. J. Changlani, R. Lamberty, and C. L. Henley (unpublished).

[49] L. Messio, B. Bernu, and C. Lhuillier, Phys. Rev. Lett. **108**, 207204 (2012).

[50] X. G. Wen, Phys. Rev. B **65**, 165113 (2002).

[51] F. Wang, Phys. Rev. B **82**, 024419 (2010); F. Wang and A. Vishwanath, *ibid.* **74**, 174423 (2006).